Journal of Asian Earth Sciences 161 (2018) 35–56

Contents lists available at ScienceDirect

Journal of Asian Earth Sciences

journal homepage: www.elsevier.com/locate/jseaes

Full length article

Nature and evolution of fluid inclusions in the Cenozoic Beiya gold deposit, SW China

Heqing Liu[a,b], Xianwu Bi[a,*], Huanzhang Lu[a,c], Ruizhong Hu[a], Tingguang Lan[a], Xinsong Wang[a], Mingliang Huang[a,b]

[a] *State Key Laboratory of Ore Deposit Geochemistry, Institute of Geochemistry, Chinese Academy of Sciences, Guiyang 550005, China*
[b] *University of Chinese Academy of Sciences, Beijing 100049, China*
[c] *University of Quebec, Chicoutimi, Quebec G7H 2B1, Canada*

ARTICLE INFO

Keywords:
Porphyry deposit
Beiya gold deposit
Fluid inclusion
LA-ICP-MS

ABSTRACT

The Beiya Au deposit in the Sanjiang metallogenic belt, SW China, is a porphyry-skarn deposit that formed in an intracontinental setting. Three stages of hydrothermal veins, namely quartz veins (Stage 1), quartz-pyrite veins (Stage 2), and Au-rich sulfide-quartz veins (Stage 3) were identified on the basis of field relationship and petrography under scanning electron microscopy cathodoluminescence (SEM-CL). Intermediate density aqueous fluid inclusions (ID1, ID2), high density brine inclusions (B1, B2), and low density vapor inclusions (V1, V2) have been identified in both Stage 1 and Stage 2 veins. Only liquid-rich fluid inclusions (L3) were found in Stage 3 veins. Raman spectroscopy revealed that all the inclusions contain abundant CO_2. H_2S was identified in ID2 and V2 inclusions. Salinities and homogenization temperatures of the intermediate density aqueous fluid inclusions (ID1, ID2), high density brine inclusions (B1, B2), and low density vapor inclusions (V1, V2) are 7.4 ± 1.1–11.9 ± 2.2, 33.6 ± 0.5–39.2 ± 1, and 1.6 ± 0.7–5.8 ± 0.8 (wt% NaCl equiv.) and 400 ± 35–440 ± 37, 395 ± 20–414 ± 6, and 386 ± 5–416 ± 4 °C, respectively. Salinities and homogenization temperatures of the L3 inclusions range from 4.9 ± 1.6 to 9.8 ± 0.7 (wt% NaCl equiv) and from 301 ± 28 to 398 ± 4 °C, respectively. Initial intermediate density aqueous fluid inclusions contain 2000–10,000 ppm Fe, 2000–4000 ppm Cu, 200–600 ppm Zn, 200–500 ppm Pb, 17–89 ppm Mo, 1–8 ppm Ag, and 0.9–5.9 ppm Au, comparable to that of intermediate density inclusions in subduction-related porphyry deposits. Brine inclusions are rich in metals and have 9000–24600 ppm Fe, 3400–11,000 ppm Cu, 1200–5200 ppm Pb, 500–3000 ppm Zn, hundreds of ppm Mo, and tens of ppm Ag. The corresponding vapor inclusions contain lower metal concentrations: 400–6000 ppm Fe, 1700–4700 ppm Cu, 50–270 ppm Pb, 100–500 ppm Zn, and minor Mo and Ag. Low to intermediate density fluids are abundant and are inferred to have been the main metal transporting medium. A temperature decrease to approximately 350 °C during Stage 3 triggered metal precipitation.

1. Introduction

Porphyry deposits typically form in subduction-related arc environments (Cooke, 2005; Sillitoe, 2010), but also in post-collisional intracontinental tectonic settings (Bi et al., 2009, 2005, 2004; Hou et al., 2009; Xu et al., 2016, 2015, 2012). In both environments, porphyry Cu deposits share similar mineralization characteristics with multiple stages of vein formation associated with mineralization (Richards, 2011; Sillitoe, 2010). Fluid inclusions trapped in gangue and ore minerals in veins of porphyry systems provide the most direct means of studying porphyry ore-forming processes because they represent micro-samples of the paleomagmatic-hydrothermal fluids responsible for ore mineral deposition (Roedder, 1967; Wilkinson, 2001). The evolution of ore-forming fluids and the mineralization processes of subduction-related porphyry deposits, have been studied using fluid inclusions (Cline, 1995; Heinrich et al., 2004; Klemm et al., 2007, 2008; Landtwing et al., 2005; Richards, 2011; Rusk et al., 2004, 2008; Ulrich et al., 2002). However, much less attention has been paid to post-collisional, intracontinental porphyry deposits (Hou et al., 2007; Wang et al., 2017), especially with respect to their fluid compositions, metal transporting media and precipitating mechanisms.

The Beiya Au deposit in the Sanjiang metallogenic belt, Southwest China, is one of the largest Au deposits in China. It has proven reserves of more than 370 tons (t) of Au with an average grade of 2.52 g/t Au, and considerable amount of Fe, Cu, Pb, Zn, and Ag reserves (He et al., 2016). The geodynamic processes (Deng et al., 2014, 2015; Fu et al.,

---

[*] Corresponding author.
E-mail address: bixianwu@vip.gyig.ac.cn (X. Bi).

https://doi.org/10.1016/j.jseaes.2018.04.034
Received 5 February 2018; Received in revised form 27 April 2018; Accepted 28 April 2018

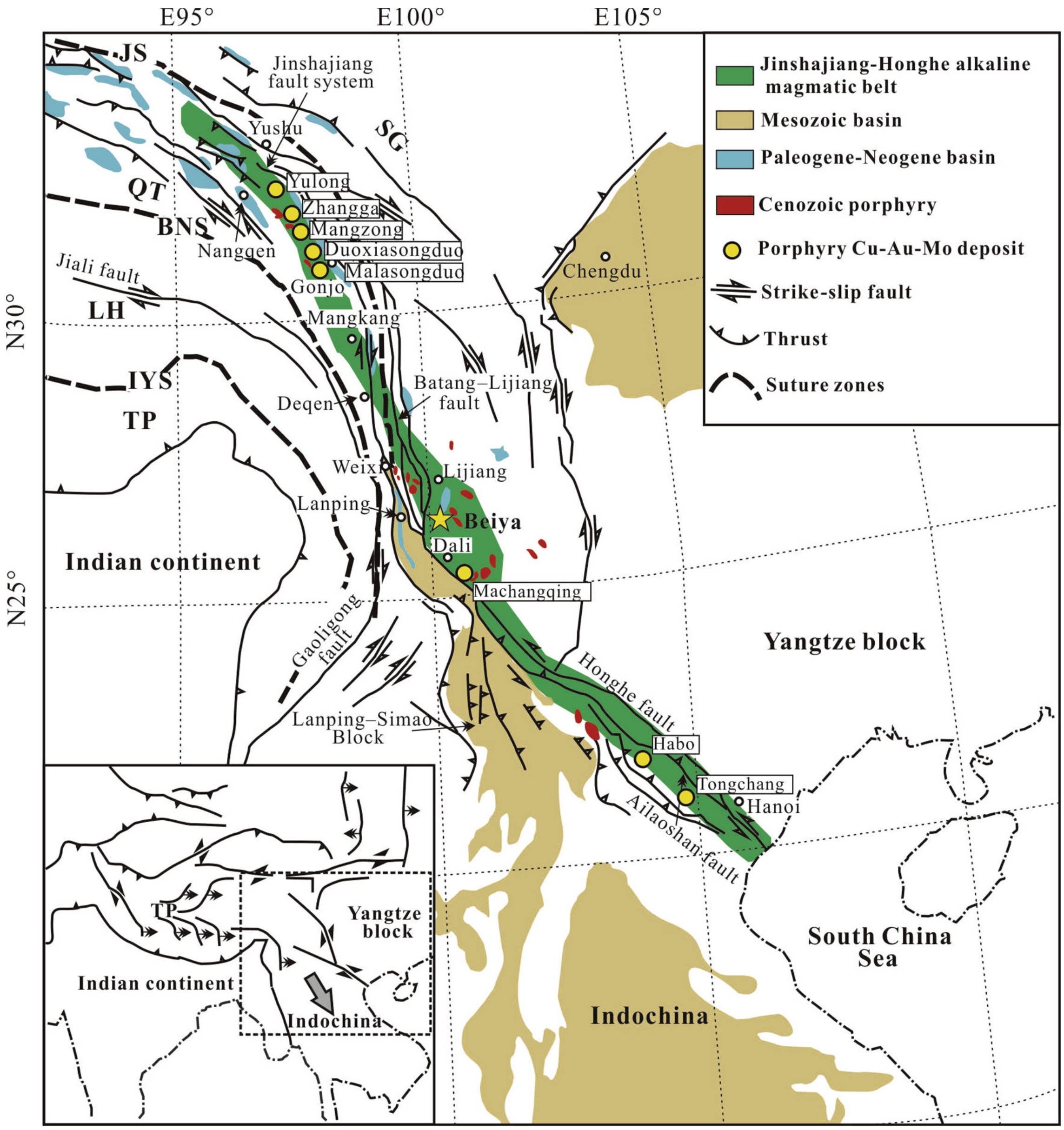

Fig. 1. Simplified geological map showing the tectonic framework and distribution of porphyry Cu-Au-Mo deposits in the Jinshajiang-Honghe alkaline magmatic belt (modified from Xu et al., 2012). The yellow star marks the location of the Beiya Au deposit. (For interpretation of the references to color in this figure legend, the reader is referred to the web version of this article.)

2015; He et al., 2015; Li et al., 2016; Liu et al., 2015; Xu et al., 2007, 2006) and mineralization styles (Fu et al., 2017, 2016; He et al., 2016, 2015; Zhou et al., 2017, 2016) of the Beiya Au deposit and related porphyry indicate that the Beiya Au deposit is a typical porphyry-skarn mineralization system in an intracontinental setting. Numerous fluid inclusions are well developed within extensive hydrothermal veins in the Beiya deposit, and provide a good opportunity for a detailed study of ore-forming fluids of a post-collisional porphyry deposit.

In this study, the characteristics and stages of mineralization within the Beiya porphyry have been studied in detail using field and microscopic methods. The evolutionary path, compositional nature, metal transporting medium, and precipitating mechanism of ore-forming fluids in the Beiya deposit have been reconstructed on the basis of fluid inclusion petrography, microthermometry, and laser ablation inductively coupled plasma mass spectrometry (LA-ICP-MS) analysis.

2. Geological setting

In the Sanjiang region, the eastern Tethyan orogen has a complex tectonic evolutionary history, including the closure of the Paleo-, Meso-, and Neo-Tethyan Oceans and subsequent amalgamation of several Gondwana-derived micro-continental blocks and Paleozoic arcs

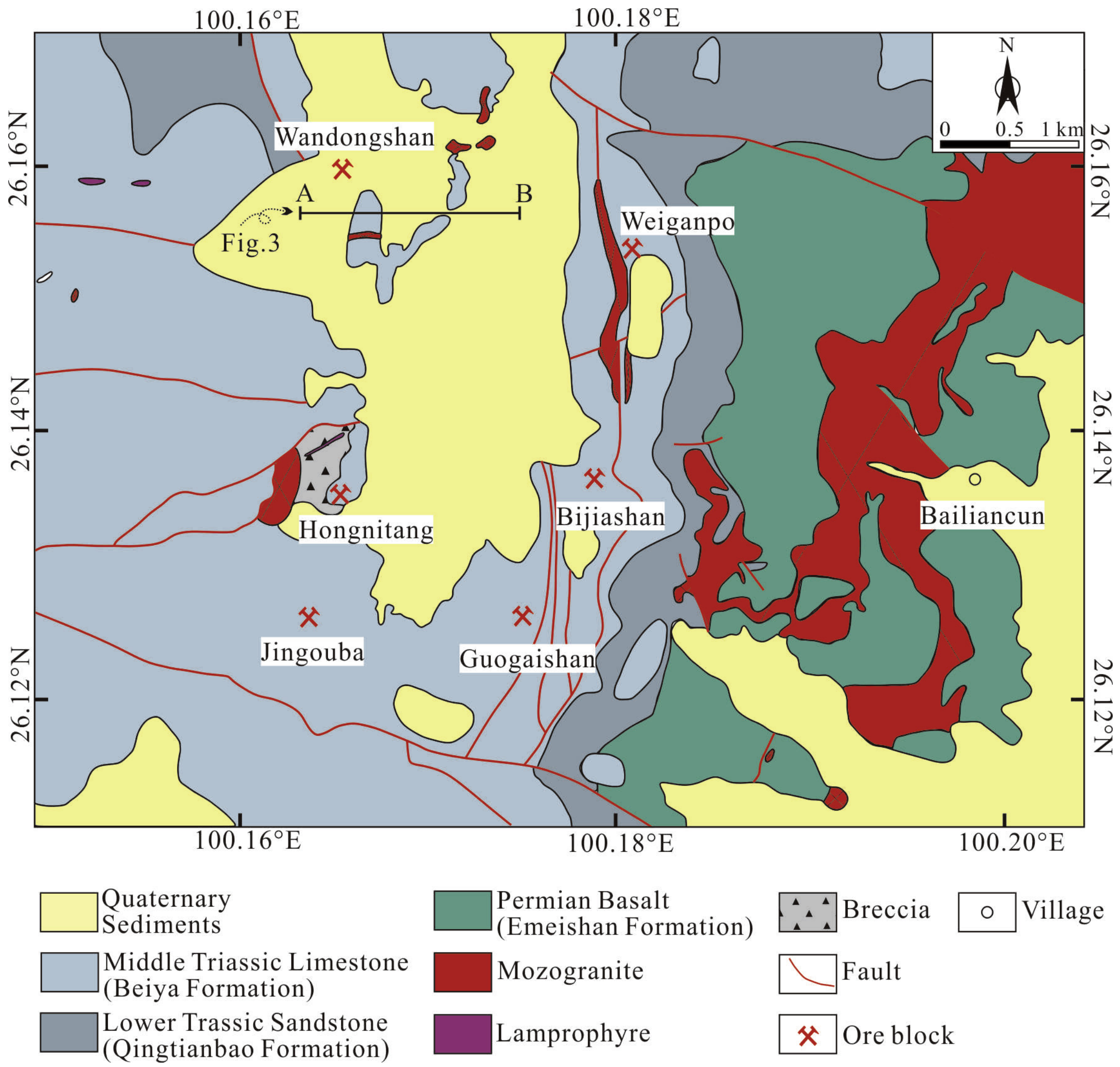

Fig. 2. Simplified geological map of the Beiya Au deposit (modified from Liu et al., 2015).

(Deng et al., 2014; Lu et al., 2013). During the Cenozoic, the India-Eurasian collision triggered a series of mantle-penetrating strike-slip fault systems and magmatism in the Sanjiang region (Deng et al., 2014; He et al., 2015; Liu et al., 2017). The Jinshajiang-Honghe fault system is one such strike-slip fault system in the east of the Sanjiang region and is associated with alkaline intrusions forming an over 2000 km long and 50–80 km wide magmatic belt (Fig. 1). In this belt, porphyry-skarn Cu-Au-Mo deposits include the Yulong, Beiya, Machangqing, Yao'an, and Habo deposits (Bi et al., 2005; He et al., 2015; Hou et al., 2004; Hu et al., 2004; Xu et al., 2016, 2015, 2014, 2012). The Beiya Au deposit is the largest of these deposits in the central part of this magmatic belt (Fig. 1).

2.1. Ore deposit geology

The geological structure in the Beiya region is characterized by nearly N-S trending faults such as the Maanshan fault, a secondary fault of the Jinshajiang-Honghe strike-slip fault system (Yang et al., 2014). The N-S Songgui syncline in the region includes a small secondary syncline named the Beiya syncline. Several ore blocks of the Beiya deposit are located in both the east and west limbs of the Beiya syncline (Fig. 2).

The regional strata mainly include three formations (Fig. 2). The Late Permian Emeishan Formation consists mainly of basalt and is overlain by the Lower Triassic Qintianbao Formation of sandstones and hornfels (Figs. 2 and 3). The overlying Beiya Formation is predominantly a fine-grained limestone with layers of siltstone and bioclastic limestone (Figs. 2 and 3). Faults and fracture zones are well developed in these carbonate rocks, and are favorable for metal precipitation (Yang et al., 2014).

In the Beiya area, the monzogranite porphyry was intruded by lamprophyre and biotite monzogranite porphyry. Monzogranite porphyry intrusions are abundant and controlled by a N-S trending regional fault system (Fig. 2). These porphyries intrude carbonate wall-

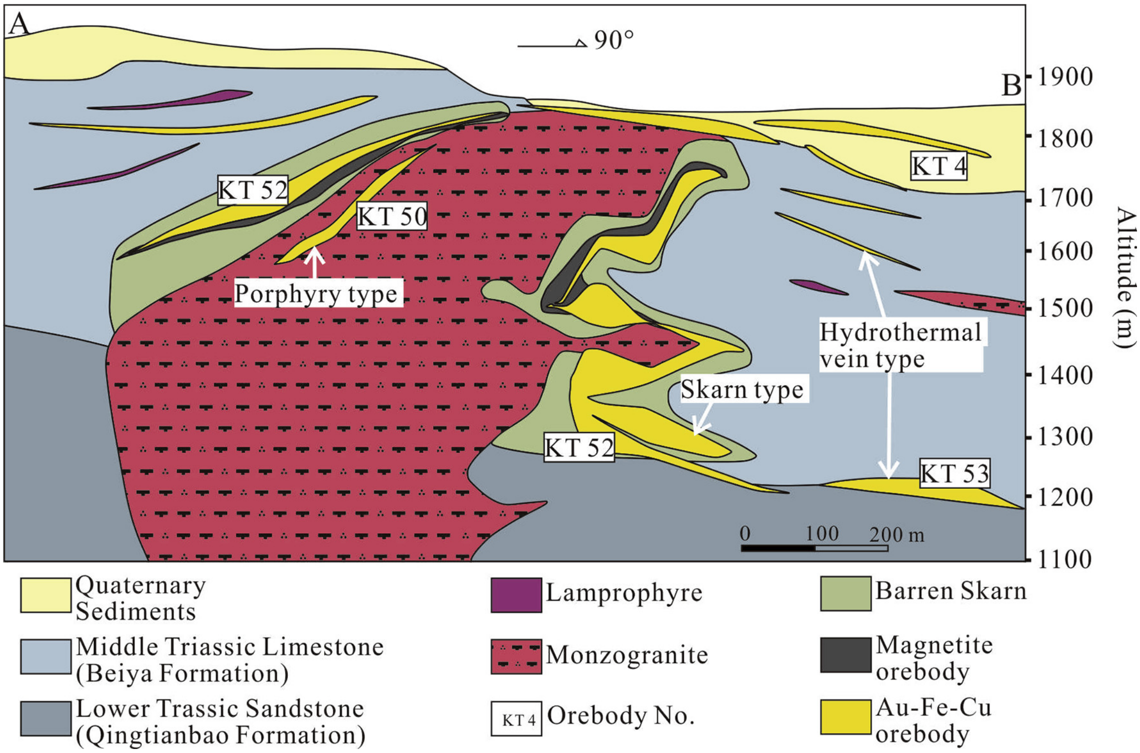

Fig. 3. Representative vertical cross-section showing the three types of mineralization in the Wandongshan ore block of the Beiya Au deposit (modified from He et al., 2015).

rocks, occur as stocks and dikes with ages of around 36 Ma (Deng et al., 2015), and are closely related to the mineralization. Minor biotite monzogranite porphyries (Fig. 4A and C) and lamprophyres crosscut monzogranite porphyries, wall rock, and orebodies (Fig. 4B–D), and are thought to have no genetic relationship with the mineralization (Xu et al., 2007, 2006).

2.2. Mineralization

The Beiya deposit comprises six ore blocks (Fig. 2): the Wandongshan, Hongnitang, and Jingouba blocks in the west limb and the Weiganpo, Bijiashan, Guogaishan blocks in the east limb (He et al., 2013). Over 400 Au-Fe-Cu-Pb-Zn-Ag mineralized zones were discovered in the mining area. There are three types of primary ore and/or mineralization in the Beiya deposit, namely porphyry type, skarn type, and hydrothermal vein type (Fig. 3).

Skarn ore bodies formed mainly at the contact zone between the porphyries and carbonate rocks of the middle Triassic Beiya Formation in the Wandongshan and Hongnitang ore blocks (e.g. KT52; Fig. 3). The thickness of the skarn ore bodies varies from less than 1 m to more than 100 m, depending on their position between porphyries and wall-rocks. The main skarn mineral is garnet, and pyroxene is uncommon. Massive magnetite ores with disseminated pyrite and chalcopyrite are the most abundant ore type. Sulfide veinlets are also common, crosscutting massive skarns and magnetite ores.

Hydrothermal Pb-Au-Ag ore bodies are distributed in fracture zones within the Beiya Formation and in the contact zone between the Beiya and Qingtianbao Formations (e.g. KT53; Fig. 3). Ore bodies are generally composed of disseminated and densely disseminated veins. The mineral assemblage comprises galena, sphalerite, pyrite, chalcopyrite and limonite with minor siderite, calcite, and dolomite (Li et al., 2016; Yang et al., 2014). These ore bodies are relatively far from porphyries and occurs in the outer zone of the area, especially in the north.

2.3. Hydrothermal stages

Based on the mode of occurrence, mineral assemblage, and alteration characteristics, there are three stages of vein formation with clear cross-cutting relationships (Table 1).

2.3.1. Stockwork quartz veins (S1) of Stage 1

Stage 1 quartz veins (S1) are widely distributed in the porphyries and are cut by all other vein types, indicating that they are the earliest vein generation (Fig. 5). S1 veins occur as stockworks with irregular wavy margins (Fig. 5A) or parallel sheeted vein swarms with planar walls (Fig. 5B). S1 veins have a granular internal texture and are composed of anhedral quartz (Fig. 7A and B). Some S1 veins have visible thin alteration halos made of K-feldspar with minor magnetite. Almost no sulfides can be found in S1 veins except rare molybdenite.

2.3.2. Quartz-pyrite vein (S2) of Stage 2

Stage 2 quartz-pyrite veins (S2) crosscut Stage 1 veins (Fig. 5C) and have more extended and straighter margins than S1 veins. S2 veins are typically 1–5 cm wide and substantially wider than S1 veins (Fig. 5C–E). Many S2 veins have a comb-like texture with subhedral-euhedral quartz crystals symmetrically from both sides of the wall

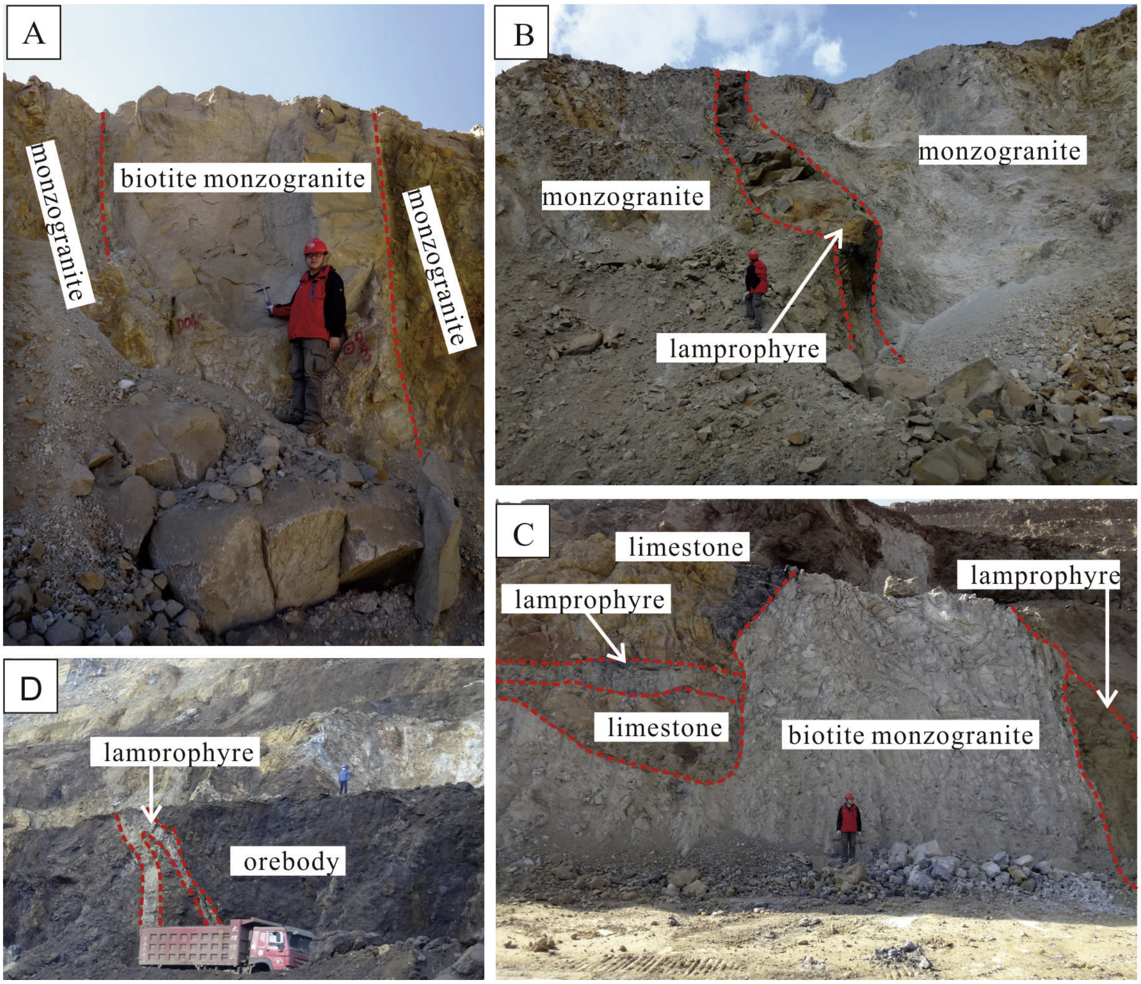

Fig. 4. Photographs of intrusions in the Beiya deposit. (A): Later biotite monzogranite porphyry intruding the earlier monzogranite porphyry; (B): Later lamprophyre crosscutting the earlier monzogranite porphyry; (C): Subsequent lamprophyre intruding limestone of the Beiya Formation and later biotite monzogranite crosscutting the lamprophyre; (D): Lamprophyre crosscutting the skarn orebody.

towards the center of the veins (Fig. 5C and D). In general, quartz in S2 veins is coarser than that in S1 veins. Some pyrite crystals are the most significant characteristic of the S2 veins (Fig. 5D). Minor molybdenite is also observed in S2 veins. S2 veins have similar alteration to S1 veins.

2.3.3. *Gold-rich sulfide-quartz vein (S3) of Stage 3*

Stage 3 Au-rich sulfide-quartz veins (S3) truncate S1 and S2 veins (Fig. 5A and E). S3 veins can be traced for several decameters along strike and are usually several centimeters wide, with stable planar margins. In many cases, long parallel S3 veins are almost vertically distributed in the porphyries, with many thinner, subordinate veins, forming interconnecting vein systems. At the contact zone, S3 veins are connected to skarn ores (Fig. 5G). In contrast to S1 and S2 veins, quartz is not the main mineral but pyrite and chalcopyrite are the most abundant minerals in S3 veins (Fig. 5F and 6). Chalcopyrite was overprinted by chalcocite and carbonaceous matter (Fig. 6B and C). Gold exists as electrum particles and is either enclosed in pyrite (Fig. 6D) or on the boundary of pyrite crystals (Fig. 6C). The main gangue minerals are adularia, gypsum, sericite, calcite, and kaolinite (Fig. 6A). Alteration assemblages include sericite, quartz, chlorite, and kaolinite. Au-rich veins comprise scattered orebodies within the porphyries.

3. Sampling and methods

The most important Wandongshan ore block in the Beiya deposit comprises more than 80% of the Au reserve of the deposit (Yang et al., 2014). It has been the main exploration target for more than five years, which has resulted in a big open pit. More than 100 samples were collected from the monzogranite porphyry within the Wandongshan open pit. Sixty four samples containing hydrothermal quartz veins were washed and made into doubly polished thin sections, with a thickness of approximately 200 μm. After detailed observations of the fluid inclusions under a petrographic microscope, eight representative sections were selected for further analysis. Among them, four samples, W15-38-1, W15-39-2, W15-40, and W15-47-1 are from S1 veins; two samples, W15-10 and W15-32-3 are from S2 veins; and two samples, W15-2 and W15-3-2 are from S3 veins (Table 1). All experiments were completed at the State Key Laboratory of Ore Deposit Geochemistry, Institute of Geochemistry, Chinese Academy of Sciences (IGCAS).

3.1. *SEM-CL*

SEM-CL was performed using a JSM-7800F type thermal field

Table 1
Stages of mineralization in the Beiya deposit and corresponding fluid inclusion types.

Stages	Stage 1	Stage 2	Stage 3
hydrothermal vein	quartz vein	quartz-pyrite vein	gold-rich sulfide-quartz veins
sample no.	W15-38-1, W15-39-2, W15-40, W15-47-1	w15-10, w15-32-3	w15-2, w15-3-2
mineralogy	quartz, molybdenite, K-feldspar	quartz, molybdenite, k-feldspar, pyrite	quartz, pyrite, chalcocite, galena, bismuthinite, adularia, gypsum, sericite, calcite, kaolinite
alteration	potassic (magnetite)	potassic (magnetite)	phyllic (sericite, quartz, chlorite)
Fluid inclusion type			
intermediate density aqueous fluid inclusion (ID)	ID1 ▬	ID2 ▬	
high density brine fluid inclusion (B)	B1 ▬	B2 ▬	
low density vapor fluid inclusion (V)	V1 ▬	V2 ▬	
liquid-rich fluid inclusion (L)			L3 ▬

scanning electron microscope from JEOL equipped with a TEAM Apollo XL energy disperse spectroscope and a Mono CL4 cathodominescence spectroscope from Gantan. After the samples were carbon-coated, cathodoluminescence (SEM-CL) images of selected samples were acquired under an acceleration voltage of 10 kV and a beam current density of 10 nA/mm. Most images presented here are mosaics of multiple CL images digitally stitched together after acquisition because of the limited field of view.

3.2. Laser Raman spectrometry

Laser Raman spectrometry was used to identify daughter minerals and qualitatively analyze volatile components in 42 fluid inclusions, representing different types and/or stages of fluid inclusion. Data were obtained using a Renishaw inVia Reflex equipped with a CCD detector and an Ar ion laser. The laser beam, with a wavelength of 514.5 nm and 20 mW power, was focused on the fluid inclusions. The spatial resolution was approximately 1 um. Spectra were collected over 60 s in a range from 100 to 4000 cm^{-1}. The aperture width was 65 um and the grating was 1800 lines cm^{-1}.

3.3. Fluid inclusion microthermometry

A Linkam THMSG600 cooling-heating stage system was used for fluid inclusion microthermometric analysis. The stage was calibrated at the triple point of CO_2 (−56.6 °C), and the freezing point of pure water (0.0 °C) with synthetic fluid inclusions to ensure the accuracy of the measurements. The precision of the temperature measurement was within 0.1 °C during freezing and 1 °C during heating. A heating rate of less than 0.1 °C/s was used for measuring ice-melting temperatures and the heating rate for homogenization temperature measurements was no more than 1 °C/s when phase transitions were approached. Overall, the melting temperature of solid CO_2, ice and/or clathrate, and the disappearance temperatures of daughter minerals and vapors were observed and recorded. However, not all types of data were obtained for every fluid inclusion due to the phase-types of the corresponding fluid inclusion and observation difficulties for some inclusions. To avoid accidental deviations caused by observations, all data were acquired on fluid inclusion assemblages in which inclusions display similar phase proportions and microthermometric behavior (Goldstein and Reynolds, 1994). Irregular relic fluid inclusions were carefully avoided during microthermometric analysis to minimize the impact of post-entrapment modification (Diamond et al., 2010). A total of 427 fluid inclusions from 60 assemblages were analysed microthermometrically. Salinities (wt% NaCl equiv.), densities, and minimum pressures of entrapment were calculated using the equations of Bodnar and Vityk (1994) and Zhang and Frantz (1987), and Flincor software (Brown and Lamb, 1989). In the case of CO_2-bearing fluid inclusions in which clathrate formed, salinities (wt% NaCl equiv.), CO_2 contents (mol.%) and densities were calculated using ICE software and equations from Bakker (1997) and Duan et al. (1992).

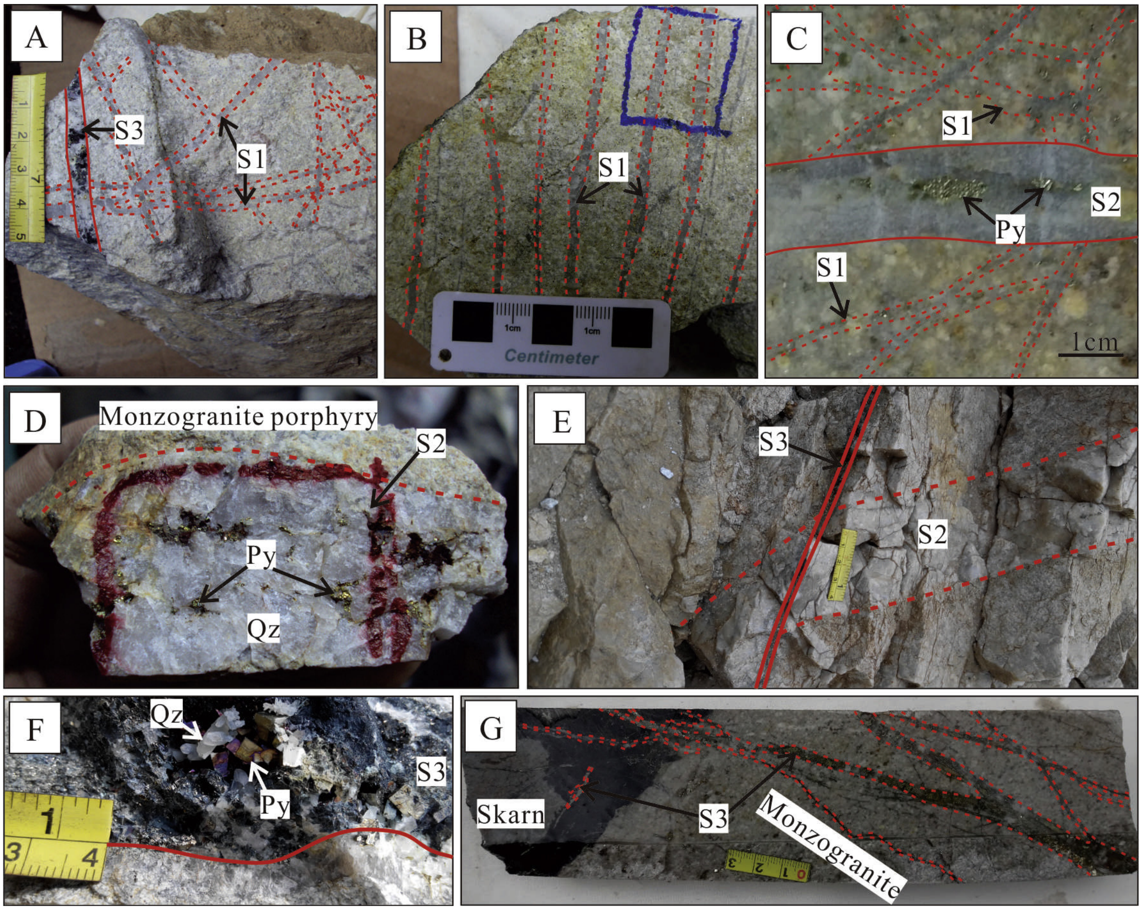

Fig. 5. Photographs of three stages of veins in the Beiya deposit. (A) Stage 1 (S1) stockwork quartz veins with irregular wavy margins, S1 veins are crosscut by S3 veins; (B) Stage 1 (S1) quartz veins occurring as a parallel sheeted vein swarm with planar walls; (C and D) Stage 2 (S2) quartz-pyrite veins cutting S1 veins and containing minor pyrite; (E) Stage 3 (S3) sulfide-quartz veins truncating S2 veins; (F) S3 vein with abundant sulfides and minor euhedral quartz; (G) S3 vein cutting earlier garnet- pyroxene skarn, forming a biotite-chlorite-magnetite alteration halo. Qz, quartz; Py, pyrite.

3.4. *Major and trace element compositions of fluid inclusions*

Individual inclusions were analyzed by laser-ablation inductively coupled plasma mass-spectrometry (LA-ICP-MS) using an Agilent 7900 ICP-MS equipped with a GeoLasPro 193 nm ArF excimer laser. The standard ablation cell was optimized with a resin mold to obtain a small volume and offer fast washout of the aerosol. Before the chamber was closed, the air was expelled by He flow. Laser repetition of 9–10 Hz and an energy density of 10–11 J/cm^2 were used during the analyses. Laser spot sizes of 24–32 μm were used for the fluid inclusion analyses, depending on the size and depth of the inclusion in quartz. The entire content of the inclusions was extracted and transported as an aerosol together with He gas. Before fluid inclusion analysis, a steady signal from NIST SRM610 glass was used to optimize the mass response and minimize oxide levels. NIST SRM610 was also used as an external standard and analyzed twice every 10 analyses. The salinity (wt% NaCl eq.) of the fluid inclusions, which was obtained independently from microthermometric analysis (see above), was used as the internal standard (Heinrich et al., 2003). Only 136 fluid inclusions (46 assemblages) from the 427 inclusions after microthermometric analysis were successfully analyzed because of fragmentation of the host quartz, decrepitation of inclusions during heating, and the unsuitable depth from the surface of the host mineral. Data collected from the ICP-MS were processed using the SILLS software (Guillong et al., 2008) for calibration, background correction, and floating of the integration signal. To ensure that the fluid inclusion signals were evaluated during this procedure without interference from the host crystal, only spectra containing signals coincident with Na and other cations were processed (Fig. 7). Moreover, for the chloride-dominated synthetic and natural fluid inclusions, the charge-balance method was applied to the microthermometric and LA-ICP-MS results (Allan, 2005). More detail can be found in Lan et al (2017a,b).

4. Results

4.1. *Cathodoluminescence textures of quartz from different veins*

S1 veins are dominated by equigranular anhedral quartz grains (S1-Q1) with high CL intensity, showing a bright gray color (Fig. 8A and B). The quartz grains have homogeneous textures and do not display

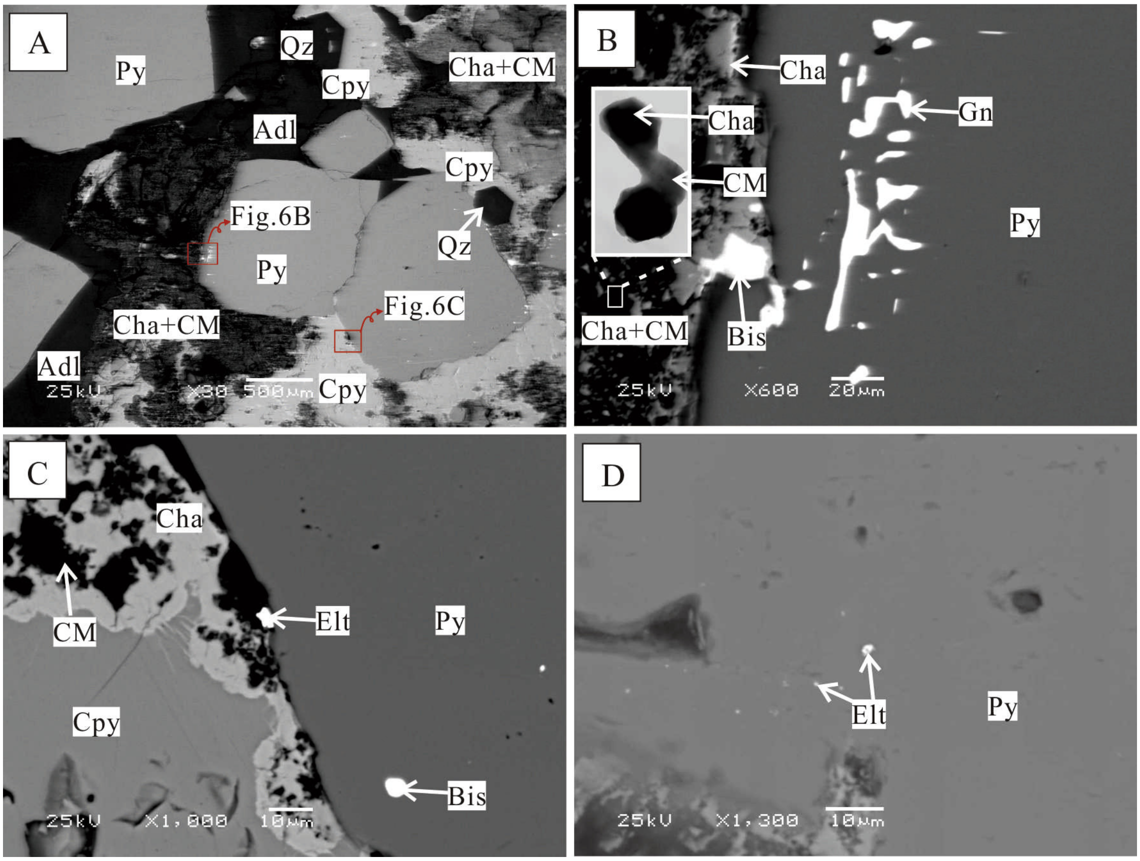

Fig. 6. BSE images illuminating the mineral assemblage of Stage 3 (S3) veins. Note that the small image in Fig. 6B was acquired by transmission electron microscope (TEM). Py, pyrite; Cha, chalcocite; Qz, quartz; Cpy, chalcopyrite; Adl, adularia; Bis, bismuthinite; Gn, galena; Elt, electrum; CM, carbonaceous matter.

internal growth zonation. Rare irregular dark patches of quartz (S1-Q2) precipitated in the interstices or fractures of these granular quartz grains, and display extremely low CL intensity (Fig. 8B).

S2 veins are mainly composed of larger sub-euhedral quartz grains (S2-Q1) (Fig. 8C and D). Unlike the S1-Q1 grains, the S2-Q1 grains show growth zones of oscillating CL intensity, with medium gray zones and bright gray zones alternating from the wall to the center of a vein (Fig. 8D). Late vein-like quartz grains (S2-Q2) cut S2-Q1 grains and are characterized by low CL intensity manifested by a black color (Fig. 8D).

S3 veins are dominated by euhedral quartz crystals (S3-Q1) with lower CL intensity than S1-Q1 and S2-Q1 crystals (Fig. 8E and F). Similar to S2-Q1 crystals, the S3-Q1 crystals show clear oscillatory growth zones with medium gray zones inter-grown with dark gray zones (Fig. 8F); some crystals also display sector zoning. Later CL-dark quartz (S3-Q2) is widely developed and occupies a considerable volume fraction of quartz in the S3 veins (Fig. 8F). The S3-Q2 crystals either form thin, irregular, and discontinuous stockwork veins in the S3-Q1 quartz or are overgrown at the boundaries of S3-Q1 crystals (Fig. 8F). There are abundant sulfide crystals with S3-Q2 crystals in fractures within the S3-Q1 crystals and in open spaces between grains.

4.2. Fluid inclusion petrography and Raman spectroscopy

Although each vein stage comprises at least two episodes of quartz, rare inclusions in S1-Q2 and S2-Q2 crystals were found. Moreover, the relative timing of the S1-Q2 and S2-Q2 crystals is not clear as they occur in different types of veins (Fig. 8B and D). Therefore, fluid inclusions in S1-Q2 and S2-Q2 crystals are not discussed here. Primary and pseudosecondary fluid inclusions in S1-Q1 and S2-Q1 crystals are thought to be the fluids from which S1 and S2 veins formed because of the simplicity of the mineral association. In S3 veins, primary fluid inclusions were rarely observed in S3-Q1 crystals due to overprinting by S3-Q2 crystals (Fig. 8F). However, numerous fluid inclusions in S3-Q2 crystals are thought to have formed simultaneously with ore minerals. Therefore, fluid inclusions in S3-Q2 crystals were analyzed to characterize the ore-forming fluids.

S1 veins contain three types of fluid inclusions (Table 1), namely intermediate density aqueous fluid inclusions (ID1), high density brine inclusions (B1), and low density vapor inclusions (V1). The ID1 inclusions comprise an aqueous phase and a vapor phase, with the latter accounting for 40–50 vol% of an inclusion at room temperatures (Fig. 9A and B). Raman spectroscopic analyses revealed that the vapors contain abundant CO_2 (Fig. 10A); in some cases, a double bubble with a liquid CO_2 phase was observed (Fig. 9E). The ID1 inclusions are

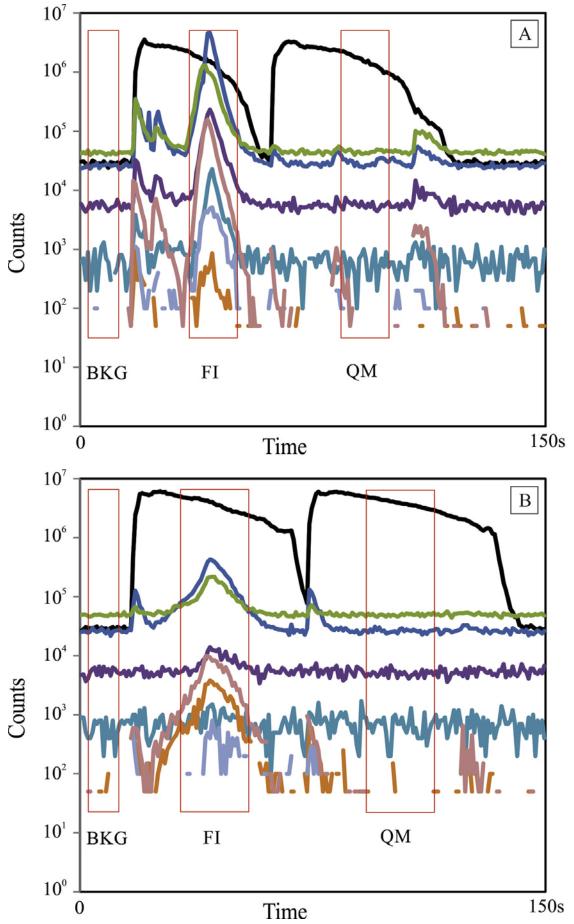

Fig. 7. Diagrams showing LA-ICP-MS signals of selected elements from a brine inclusion (A) and an intermediate density aqueous fluid inclusion (B). BKG, background signal; FI, fluid inclusion signal; QM, quartz matrix signal.

typically 10–20 μm in diameter with negative crystal or elliptical shapes and randomly distributed in S1-Q1 crystals. Pyrite and/or chalcopyrite in many ID1 inclusions were observed under Raman spectroscopy. The B1 inclusions typically coexist with V1 inclusions as clusters or on pseudosecondary trails in S1-Q1 crystals, indicating boiling. However, the proportion of B1 inclusions is substantially smaller than that of V1 inclusions. The B1 inclusions with negative crystal shapes contain a small bubble (10–20 vol%), a halite cube, and an aqueous phase (Fig. 9C). Raman spectroscopic analyses indicate that the small vapor bubble of B1 inclusions contains CO_2 and occasionally pyrite and/or chalcopyrite (Fig. 10C). In some cases, transparent minerals, such as calcite and sylvite, co-exist with halite. The V1 inclusions with negative crystal shapes contain a large vapor bubble (60–90 vol%), a small portion of aqueous phase (Fig. 9D), and occasionally a chalcopyrite and a liquid CO_2 phase. Similar to ID1 inclusions, V1 inclusions contain substantial CO_2 gas (Fig. 10B).

S2 veins contain fluid inclusions similar to that in S1 veins (Table 1), namely intermediate density aqueous fluid inclusions (ID2), high density brine inclusions (B2), and low density vapor inclusions (V2). The characteristics of each type of inclusion in the S2 vein are comparable to corresponding inclusion types in the S1 veins (Fig. 9F–H). However, considerable H_2S was identified by Raman spectroscopy in ID2 and V2 inclusions in S2 veins (Fig. 10C and D). Boiling assemblages comprising B2 and V2 inclusions are mainly present in pseudosecondary trails of S2-Q1 crystals. The B2 inclusions also contain pyrite and/or chalcopyrite (Fig. 10E). The abundance of brine inclusions in S2-Q1 crystals is smaller than that in S1-Q1 crystals.

S3 veins only comprise liquid-rich fluid inclusions (L3) with relatively small vapor bubbles (20–40 vol%) (Fig. 9I), containing obvious CO_2 (Fig. 10F). The L3 inclusions are distributed along S3-Q2 crystals. L3 inclusions are typically 10–20 μm in diameter with irregular shape. The relative timing of fluid entrapment from early to late stages is ID1 ≥ B1 = V1 > ID2 ≥ B2 = V2 > L3.

4.3. Microthermometric results

Table 2 presents the microthermometric data as averages for fluid inclusion assemblages with 1σ uncertainty (Figs. 11 and 12). In general, most of the two-phase inclusions at room temperatures, including ID1, V1, ID2, V2, and L3 inclusions, formed a drikold when frozen to −100 °C, and a melting point was observed after reheating to almost −56.6 °C. A CO_2 clathrate was detected in most of these inclusions, with a disappearance temperature above 0 °C, which indicates a high CO_2 content in the fluids, as suggested by Raman analysis. The ice melting temperature could only be detected in a small proportion of these two-phase inclusions because of the difficulties to observe. During heating, the halite crystal disappeared before the bubble for all halite-bearing inclusions. The homogenization temperature of some extremely vapor-rich inclusions was not obtained because of the difficulties to observe.

The drikold of ID1 and V1 inclusions from Stage 1 veins melted between −56.6 ± 0.1 and −56.9 ± 0.1 °C, indicating nearly pure CO_2 gas. The ice-melting temperatures of ID1 inclusions are lower than those of V1 inclusions, and range from −4.8 ± 0.6 to −7.9 °C and from −1.6 to −3.9 ± 1.8 °C for ID1 and V1, respectively. The clathrate melting temperatures of ID1 inclusions and V1 inclusions range from 3.2 ± 0.6 to 6.0 ± 0.8 °C and from 7.0 ± 0 to 8.8 ± 0.7 °C, respectively. Calculated salinities of ID1 inclusions and V1 inclusions are 7.5 ± 1.2–11.7 ± 0.1 and 2.3 ± 1.3–5.7 ± 1.8 wt% NaCl equiv., respectively (Figs. 11 and 12). The total homogenization of ID1 inclusions occurred close to the critical point (fading meniscus) or by vapor bubble disappearance into the liquid phase at 402 ± 18–440 ± 14 °C. The V1 inclusions homogenized to vapor at 390 ± 17–412 ± 5 °C (Table 2; Figs. 11 and 12). According to halite-disappearing temperatures at 270 ± 10 ~ 312 °C, calculated salinities of B1 inclusions range from 35.9 to 38.9 wt% NaCl equiv. Total homogenization of B1 inclusions occurred by bubble disappearance at 408 ± 20–414 ± 6 °C (Table 2; Figs. 11 and 12).

In Stage 2 veins, the drikold melting temperatures of ID2 and V2 inclusions (56.6 ± 0.1–58.6 ± 0.1 °C) are lower than those of ID1 and V1 inclusions, indicating that CO_2 gas is accompanied by a minor proportion of other gas species. This is consistent with the presence of H_2S in the vapors of ID2 and V2 inclusions as shown by Raman analysis. Similar to the situation in S1 veins, the ice-melting temperatures of ID2 inclusions (−3.7 ± 0.6 to −9 ± 1.0 °C) are lower than those of V1 inclusions (−1.1 ± 0.4 to −3.5 °C), and the clathrate melting temperatures of ID2 inclusions (2.9 ± 1.6 ~ 6.0 ± 0.7 °C) are lower than those of V2 inclusions (7.0 ± 0.4 ~ 9.2 ± 0.4 °C). The calculated salinities of ID2 and V2 inclusions range from 7.4 ± 1.1 to 11.9 ± 2.2

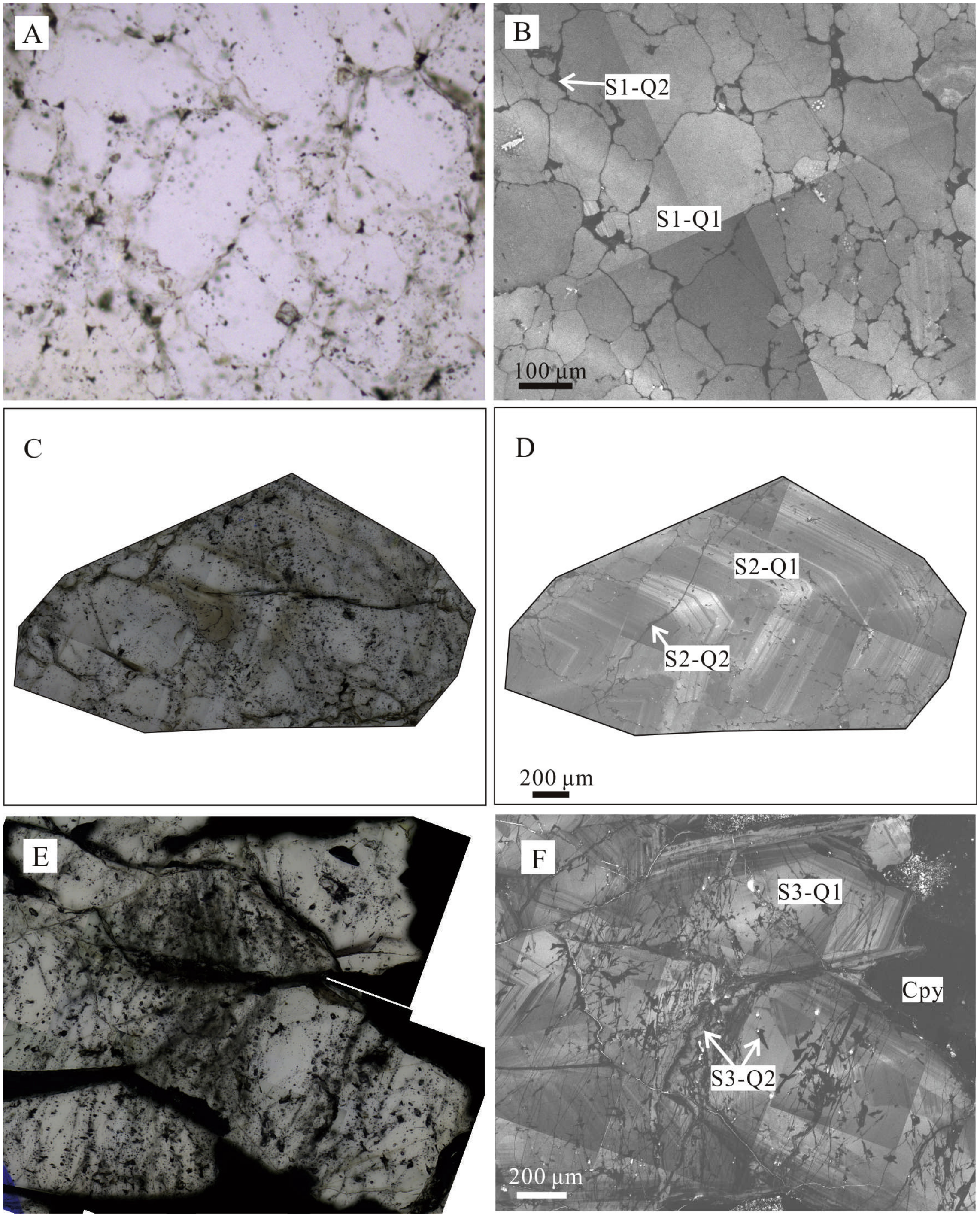

Fig. 8. Optical microscope (A, C and E) and SEM-CL (B, D and F) images of quartz from Stage 1 (A and B), Stage 2 (C and D), and Stage 3 (E and F) veins in the Beiya deposit. See text for detailed descriptions.

and from 1.6 ± 0.7 to 5.8 ± 0.8 wt% NaCl equiv., respectively (Table 2; Figs. 11 and 12). The homogenization behaviors of ID2 (400 ± 35–440 ± 37 °C) and V2 inclusions (386 ± 5–416 ± 4 °C) were also similar to that of ID1 and V1 inclusions, respectively, except that ID2 inclusions displayed a wider range of homogenization temperatures (Table 2; Figs. 11 and 12). The salinities of B2 inclusions are between 34.9 and 39.2 wt% NaCl equiv. according to halite-melting temperatures of 247 ± 69–316 ± 2 °C. The B2 inclusions are homogenized at 395 ± 20–409 ± 14 °C by vapor disappearance.

The drikold of L3 inclusions from Stage 3 veins decomposed between −56.6 ± 0.1 and −57.3 ± 0.1 °C, indicating rare impurities of CO_2 gas, although no other gas species were detected in the Raman spectra.

Clathrates of L3 inclusions decomposed at 4.5 ± 0.5 to

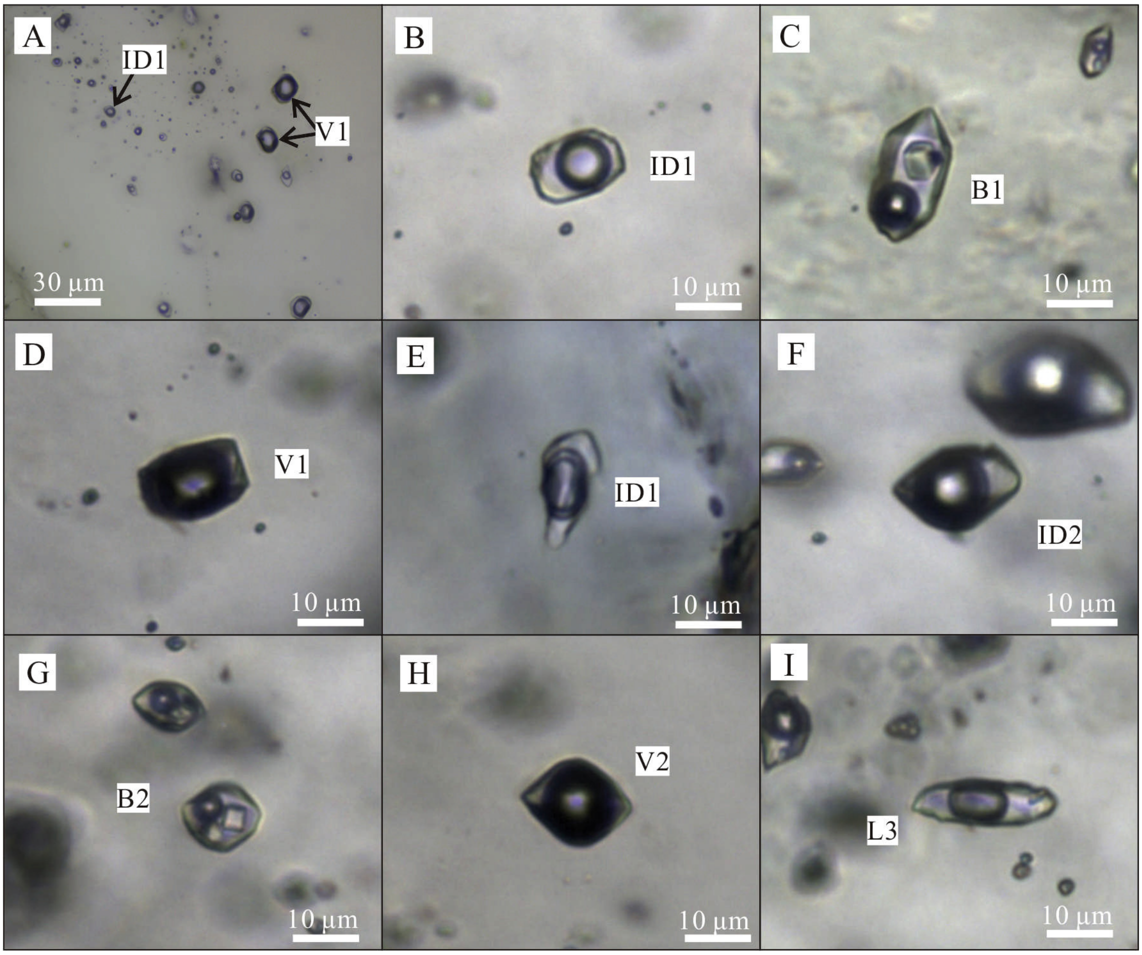

Fig. 9. Optical microscope photographs of fluid inclusions from Stage 1 (A–E), Stage 2 (F–H), and Stage 3 (I) veins in the Beiya deposit. See text for detailed descriptions.

7.2 ± 0.9 °C. Calculated salinities range from 4.9 ± 1.6 to 9.8 ± 0.7 wt% NaCl equiv. All L3 inclusions were homogenized by the disappearance of vapor at 301 ± 28–398 ± 4 °C, the lowest homogenization temperatures among all types of fluid inclusions (Table 2; Figs. 11 and 12).

The calculated densities, CO_2 contents, and minimum pressures for ID1 and ID2 inclusions are comparable (Table 2), with intermediate densities (0.48–0.67 g/cm^3), intermediate CO_2 contents (3.30–4.66 mol.%), and the highest minimum pressures (271–395 bar). The B1 and B2 inclusions also have similar properties, with high densities of 0.96–0.99 g/cm^3. The V1 and V2 inclusions have similar low densities (0.34–0.39 g/cm^3) and high CO_2 contents (6.42–10.62 mol.%). These two boiling assemblages have similar minimum entrapment pressures of approximately 300 bar. Densities of L3 inclusions range between 0.62 and 0.82 g/cm^3. L3 inclusions have 3.38–4.72 mol.% CO_2 content, comparable to ID1 and ID2 inclusions. However, L3 inclusions have the lowest pressure of 83–266 bar.

4.4. LA-ICP-MS results

A total of 30 elements, namely Li, Na, Mg, Al, Si, S, Cl, K, Ca, Ti, V, Cr, Mn, Fe, Cu, Zn, Ge, As, Rb, Sr, Mo, Ag, Sn, Sb, Cs, Ba, W, Au, Pb, and Bi, were analyzed. However, the concentrations of many elements (e.g. Mg, Al, Si, S, Cl, Ca, Ti, V, Cr, Ge, As, Sn, and Au) were below the detection limits for most inclusions. Selected element data are presented in Table 3 as averages for fluid inclusion assemblages with 1σ uncertainties. Generally, fluids of the Beiya deposit contain high concentrations of Na (6566–106277 ppm), K (2829–44739 ppm), Fe (< 1297–20742 ppm), and Cu (119–10127 ppm). There are smaller amounts of Mn (< 411–4995 ppm), Pb (48–3280 ppm), Zn (77–2180 ppm), Rb (< 87–587 ppm), Sr (3–393 ppm), Cs (6–691 ppm), Ba (< 1–328 ppm), Mo (< 2–275 ppm), Ag (< 1–22 ppm), and Bi (< 1–38 ppm). Only eight analyses have Au signals with Au concentrations of 0.2–5.9 ppm.

The brine inclusions (B1, B2) contain the highest absolute concentrations of most elements (Table 3). The intermediate density aqueous fluid inclusions (ID1, ID2) contain slightly higher major element concentrations of Na, K, Fe and Mn than the vapor inclusions (V1, V2); however, the concentrations of other elements in ID1, ID2, V1, and V2 inclusions are indistinguishable from each other. The concentrations of many elements in L3 inclusions are comparable to these in the other types of inclusion. However, the Cu concentration of L3 inclusions is an order of magnitude lower, at only 119–559 ppm Cu. Another distinction is that almost all Mo, Ag, and W contents in L3 inclusions are below the detection limit. To avoid the effect of the internal standard of salinity, the M/(Na + K) ratio is used for further discussion (Figs. 14 and 15),

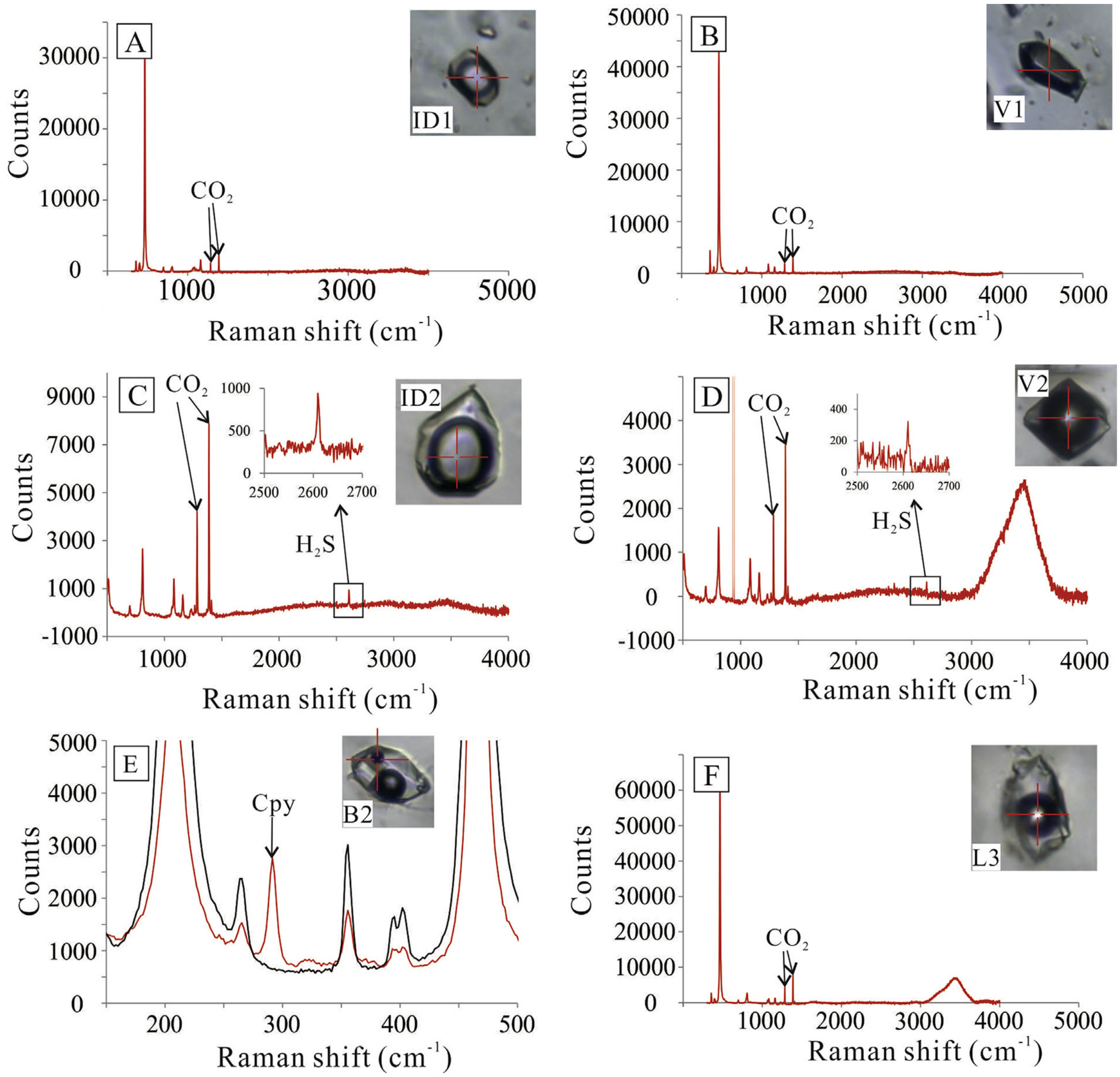

Fig. 10. Diagrams showing Raman spectra characteristics of fluid inclusions from Stage 1 (A and B), Stage 2 (C–E), and Stage 3 (F) veins; Note the abundant CO_2 in the Beiya ore-forming hydrothermal system and the existence of H_2S in fluid inclusions from Stage 2 veins (C and D).

where M is the elemental concentration and (Na + K) is the sum of the corresponding Na and K concentrations.

5. Discussion

5.1. P-T-salinity evolution of fluids

The salinity, pressure, and temperature evolution of hydrothermal fluids in the Beiya deposit was reconstructed on the basis of fluid inclusion microthermometry (Fig. 13). Intermediate density aqueous fluid inclusions (ID1) of Stage 1 stockwork quartz veins (S1) have moderate salinities (ca. 10% NaCl equiv.), and high homogenization temperatures of 400–440 °C, typical of intermediate density fluid inclusions reported for well-studied subduction-related porphyry deposits such as the Bingham (Landtwing et al., 2005), El Teniente (Klemm et al., 2007), Bajo de la Alumbrera (Ulrich et al., 2002), and Butte deposits (Rusk et al., 2008). ID1 inclusions represent the earliest fluids exsolved from the crystallizing magma in the Beiya magmatic-hydrothermal system. The estimated minimum pressure of these early fluids is 300–400 bar (Fig. 13); however, the entrapment pressures of ID1 inclusions were probably considerably higher, as these types of fluid exsolve from a deep magmatic source (Audétat et al., 2008; Hedenquist et al., 1998; Heinrich, 2007; Klemm et al., 2007; Rusk et al., 2008). Ascent accompanied cooling and decompression of ID1 inclusions in the single-phase field caused fluids to intersect the two-phase surface close to the critical curve on the liquid-like side of the two-phase surface (Fig. 13). This process led to condensation of a small amount of hypersaline brines (B1) with high salinity (ca. 35% NaCl equiv.), leaving residual vapor fluids with lower salinity (2–5% NaCl equiv.) at ca. 400 °C and 300 bar, corresponding to ca. 1.5 km lithostatic pressure. Because of pre-entrapment contamination of vapor with brine (due to the preferred wetting properties of brine relative to vapor on quartz), vapor

Table 2
Microthermometric data of fluid inclusion assemblages from three different stages of mineralization.

FIA No.	LA[1]	Tm-CO$_2$[2] (°C)	SD(N)[3]	Tm-ice[4] (°C)	SD(N)	Tm-clath[5] (°C)	SD(N)	Tm-H[6] (°C)	SD(N)	Th[7] (°C)	SD(N)	Mode[8]	Salinity[9] (wt%)	SD(N)	Density (g/cm^3)	CO$_2$[10] (mol.%)	Pressure[11] (Bar)
ID1																	
W15-38-1(6)a	X	−56.6	(1)	−6.9	1.0(4)	4.0	1.5(8)			440	14(8)	L/C	10.4	2.1(8)	0.67	3.30	395
W15-38-1(4)a	X	−56.5	0.1(2)	−5.1	0.4(2)	5.6	0.3(3)			434	17(3)	L	8.1	0.5(3)	0.65	3.91	374
W15-39-2(6)a	X	−56.8	0.1(4)	−6.6	(1)	4.0	0.9(5)			432	6(5)	L/C	10.4	1.3(5)	0.48	4.59	367
W15-39-2(5)a	X	−56.9	(1)	−6.1	0.1(2)	5.1	0.2(3)			429	24(5)	L	9.0	0.4(5)	0.61	4.07	358
W15-39-2(4)a	X	−56.9	0.1(5)	−5.8	1.7(6)	4.9	1.4(11)			415	34(13)	L/C	9.0	2.1(13)	0.65	3.75	314
W15-40(3)a	X	−56.6	0.1(2)	−7.9	(1)	3.2	0.1(2)			431	1(2)	C	11.7	0.1(2)	0.52	4.03	364
W15-40(1)a	X	−56.7	0.1(4)	−4.8	0.6(3)	6.0	0.8(15)			409	26(17)	L/C	7.5	1.2(17)	0.61	4.50	296
W15-47-1(2)a	X	−56.9	0.1(7)	−6.7	0.8(2)	4.4	0.8(8)			408	7(8)	L	10.0	1(8)	0.64	3.57	294
W15-47-1(4)a	X	−56.8	0.1(5)	−5.3	1.3(2)	5.3	1.1(6)			402	18(6)	L	8.5	1.7(6)	0.60	4.21	277
B1																	
W15-38-1(6)b	X							270	10(3)	408	6(3)	L	35.9	0.6(3)	0.96		294
W15-38-1(5)a	X							233	8(3)	414	6(3)	L	33.6	0.5(3)	0.93		311
W15-39-2(5)b	X							312	(1)	409	(1)	L	38.9	(1)	0.99		296
W15-40(1)b	X							303	24(4)	408	20(4)	L	38	2(4)	0.98		294
V1																	
W15-38-1(6)c		−56.6	0.1(6)	−3.0	0.6(6)	7.4	0.4(6)			406	11(6)	V	5.0	0.7(6)	0.48	6.84	288
W15-38-1(5)b		−56.6	0(3)	−1.7	0.3(2)	8.9	0.2(3)			390	2(3)	V	2.3	0.3(3)	0.44	8.72	245
W15-38-1(4)b		−56.5	0(2)	−2.7	(1)	7.0	1.1(2)			412	4(2)	V	5.7	1.8(2)	0.39	8.23	305
W15-39-2(6)b	X	−56.8	0.1(7)	−2.7	1.3(2)	8.0	1.4(7)			390	17(6)	V	3.9	2.5(7)	0.42	8.34	245
W15-39-2(5)c		−56.9	0(3)	−1.6	(1)	7.9	1(4)			400	7(4)	V	4.0	1.8(4)	0.47	7.38	271
W15-39-2(4)b				−3.1	(1)	7.7	0.4(2)			407	3(2)	V	4.5	0.6(2)	0.39	8.77	291
W15-40(3)b		−56.6	0.1(4)	−3.9	1.8(2)	7.7	0.2(4)			412	5(4)	V	4.4	0.3(4)	0.47	6.99	305
W15-40(1)c	X	−56.6	0.1(3)	−2.2	0.8(2)	7.9	0.6(7)			410	9(7)	V	4.1	1.2(7)	0.47	7.35	299
W15-47-1(3)a	X	−56.9	0.1(7)	−2.8	(1)	8.8	0.7(6)			391	2(4)	V	2.3	1.3(6)	0.39	9.71	248
W15-47-1(2)b	X	−56.9	0.1(4)	−3.0	(1)	7.9	1.3(4)			411	3(4)	V	4.1	2.4(4)	0.46	7.49	302
W15-47-1(4)b	X	−56.8	0.1(23)	−2.6	1.3(2)	7.9	0.9(23)			411	15(23)	V	4.1	1.6(23)	0.41	8.47	302
ID2																	
W15-10(1)a	X	−56.8	0.2(5)	−6.3	0.7(2)	5.3	1.2(11)			400	35(11)	L/C	8.5	1.9(11)	0.56	4.52	271
W15-10(7)a	X	−58.2	0.1(14)	−5.5	1.4(4)	4.4	1.3(18)			431	37(18)	L/C	9.8	1.9(18)	0.61	3.76	364
W15-10(7)d	X	−58.3	0.1(14)	−6.9	0.7(4)	3.8	1.1(17)			440	37(18)	L/C	10.7	1.5(18)	0.63	3.53	395
W15-10(7)g	X	−58.5	0.1(17)	−7.2	0.1(2)	2.9	1.6(20)			436	49(21)	L/C	11.9	2.2(21)	0.59	3.41	381
W15-10(7)i	X	−58.6	0.1(6)	−6.8	0.6(2)	4.5	0.9(11)			413	58(11)	L/C	9.7	1.4(11)	0.59	3.91	308
W15-10(7)k	X	−58.7	0.1(6)	−9.0	1(2)	4.0	2(12)			409	43(12)	L/C	10.3	3(12)	0.62	3.55	296
W14-32-3(2)a	X	−56.7	0.1(5)	−7.6	(1)	4.4	0.7(6)			410	22(6)	L/C	9.8	1(6)	0.55	4.15	299
W14-32-3(2)c	X	−56.7	0(2)	−3.7	0.6(2)	5.8	1(5)			401	28(6)	L	7.5	1.5(6)	0.66	3.99	274
W14-32-3(3)a	X	−56.6	0.1(4)	−5.1	0.1(3)	6.0	0.7(9)			424	17(10)	L	7.4	1.1(10)	0.59	4.66	342
W14-32-3(3)d	X	−57.2	0.1(4)	−6.3	2.9(2)	4.2	1.8(8)			407	24(8)	L	10.1	2.7(8)	0.54	4.17	291
B2																	
W15-10(7)b	X							247	69(6)	395	20(6)	L	34.9	4(6)	0.96		258
W15-10(7)e	X							263	64(7)	409	8(7)	L	35.9	4(7)	0.96		296
W14-32-3(3)b	X							316	2(10)	409	14(10)	L	39.2	1(10)	0.99		296
V2																	
W15-10(1)b	X	−56.9	0.1(6)	−1.1	0.4(2)	8.1	1.2(15)			393	21(15)	V	3.6	2.3(15)	0.48	7.38	253
W15-10(7)c		−58.2	0.1(3)	−1.5	(1)	9.2	0.4(3)			386	5(3)	V	1.6	0.7(3)	0.40	10.18	235
W15-10(7)f	X	−58.2	0.1(5)	−2.7	0.6(2)	8.3	1.4(7)			402	14(7)	V	3.5	2.4(8)	0.34	10.62	277
W15-10(7)h	X	−58.6	0.1(9)	−2.4	1.1(2)	7.7	1.3(9)			409	16(9)	V	4.4	2.3(9)	0.45	7.56	296
W15-10(7)j	X	−58.7	0.1(6)	−3.5	(1)	7.0	0.4(6)			414	20(6)	V	5.8	0.8(6)	0.49	6.42	311
W15-10(7)l	X	−58.7	0(2)	−2.2	(1)	7.5	0.8(2)			416	14(2)	V	4.8	1.5(2)	0.42	8.00	317
W14-32-3(2)b	X	−56.6	0.1(5)	−2.0	(1)	8.5	0.8(7)			396	19(7)	V	2.9	1.6(7)	0.44	8.37	261
W14-32-3(2)d		−56.6	0(3)	−2.4	(1)	7.6	0.8(3)			408	15(3)	V	4.6	1.4(3)	0.37	9.22	294
W14-32-3(3)c		−56.6	0.1(3)	−1.9	(1)	8.8	1.0(3)			400	8(4)	V	3.3	0.7(3)	0.42	9.05	271
W14-32-3(3)e	X	−57.2	0.1(4)	−2.7	(1)	8.0	0.4(5)			386	3(5)	V	3.9	0.7(5)	0.46	7.58	235
L3																	
W15-2(2)a				−3.0	1.1(7)	6.5	0.3(2)			301	28(7)	L	4.9	1.6(7)	0.80	3.47	83
W15-2(2)b	X	−57.3	0.1(5)	−5.7	0.2(3)	5.8	0.8(10)			356	15(10)	L	7.8	1.3(10)	0.66	3.97	169
W15-2(1)a		−57.2	(1)	−4.9	0.4(5)	6.0	1(9)			326	14(11)	L	7.5	1.6(11)	0.70	3.74	117
W15-2(1)b		−56.5	(1)	−5.3	1.2(5)	6.5	1.1(12)			333	23(15)	L	6.8	2(15)	0.63	4.54	128
W15-2(1)c				−3.8	1.2(2)	6.7	1.4(4)			342	3(4)	L	6.1	2.5(4)	0.62	4.72	143
W15-3-2(1)a	X	−56.7	0(7)	−3.6	0.4(2)	7.1				347	9(7)	L	5.5	0.6(7)	0.66	4.57	152
W15-3-2(1)b	X	−56.7	0(7)	−5.5	(1)	5.5	0.7(7)			370	16(7)	L	8.1	1.2(7)	0.67	3.75	198
W15-3-2(4)a	X			−4.1	(1)	7.4	0.3(2)			365	24(3)	L	5.5	1(3)	0.66	4.60	188
W15-3-2(5)a	X	−56.6	0.1(4)	−2.4	(1)	4.5	0.5(5)			398	4(5)	L	9.8	0.7(5)	0.70	3.38	266
W15-3-2(5)b	X	−56.6	(1)	−4.1	0.6(2)	6.9	0.6(5)			338	8(5)	L	5.9	1(5)	0.82	3.48	136
W15-3-2(5)c	X	−56.6	(3)	−7.0	(1)	6.8	1.9(4)			350	9(4)	L	5.9	3.2(4)	0.67	4.34	158
W15-3-2(5)d		−56.7	(1)	−3.2	(1)	7.2	0.9(4)			327	14(4)	L	5.3	1.6(4)	0.67	4.50	118

(*continued on next page*)

Table 2 (*continued*)

FIA No.	LA[1]	Tm-CO_2[2] (°C)	SD(N)[3]	Tm-ice[4] (°C)	SD(N)	Tm-clath[5] (°C)	SD(N)	Tm-H[6] (°C)	SD(N)	Th[7] (°C)	SD(N)	Mode[8]	Salinity[9] (wt%)	SD(N)	Density (g/cm^3)	CO_2[10] (mol.%)	Pressure[11] (Bar)
W15-3-2(5)e	X			−4.4	(1)	6.1	1.8(3)			347	13(3)	L	7.1	2.9(3)	0.68	4.03	152

Data are reported as assemblage averages.

[1] LA: Corresponding FIA was conducted via LA-ICP-MS analysis when marked with an "X".

[2] Tm-CO_2: Melting temperature of drikold.

[3] SD(N): Standard deviation (SD) and the number of inclusion per assemblage (N).

[4] Tm-ice: Ice melting temperature.

[5] Tm-clath: Melting temperature of clathrate of CO_2-H_2O.

[6] Tm-H: Halite melting temperature.

[7] Th: Total homogenization temperature.

[8] Mode: Mode of total homogenization; L (into liquid); V (into vapor); L/C (into liquid or near critically).

[9] Salinity: Calculated salinity (wt% NaCl equivalent).

[10] CO_2: Calculated CO_2 content in mole percent.

[11] Pressure: Calculated minimum pressure of entrapment.

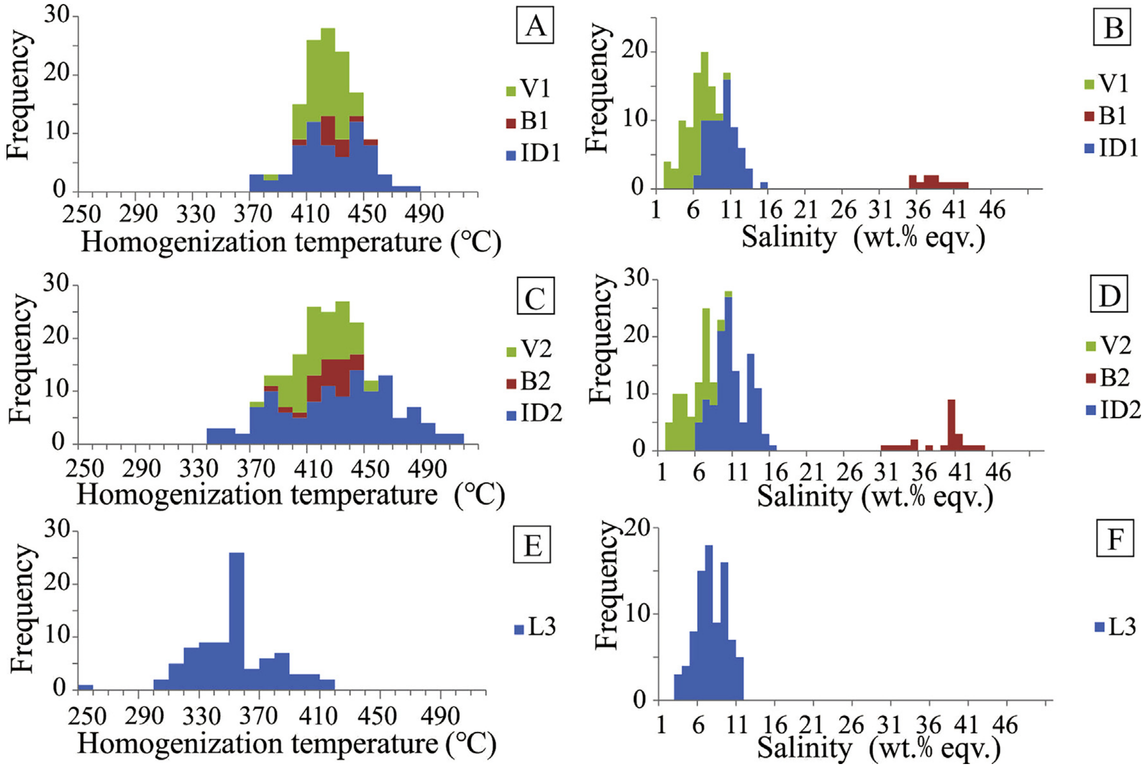

Fig. 11. Frequency histograms showing the homogenization temperatures (A, C and E) and calculated salinities (B, D and F) of fluid inclusions from Stage 1 (A and B), Stage 2 (C and D), and Stage 3 (E and F) veins.

inclusions commonly have higher salinities than predicted by the binary H_2O-NaCl phase diagram (Klemm et al., 2007). The CO_2 content in V1 inclusions (ca. 8 mol.%) is approximately twice that in ID1 inclusions (ca. 4 mol.%) due to the fact that CO_2 was enriched in the vapor (V1) during phase separation (c.f. Rusk et al., 2008).

The fluid type, salinity, CO_2 content, temperature, pressure, and evolution path in Stage 2 quartz-pyrite veins (S2) were very similar to those in S1 veins (Figs. 12 and 13), suggesting that these two types of vein formed via the same process through the same fluid source. However, the homogenization temperatures of some ID2 inclusions are higher than that of ID1 inclusions, and the homogenization temperatures of ID2 inclusions display a wider range than that of ID1 inclusions (Figs. 12 and 13). This phenomenon may have been caused by locally pulsed fluid activities in S2 veins. These repeated processes were controlled by intermittent hydraulic fracturing, alternating with chemical sealing by vein mineral precipitation. The temperature and pressure of the hydrothermal fluids fluctuated during the formation of S2 veins, resulting in some higher and/or lower homogenization temperatures of

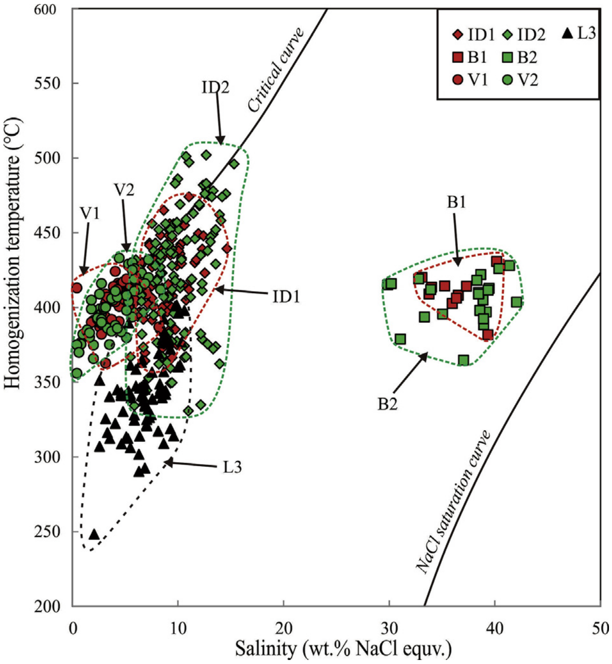

Fig. 12. Binary diagram showing homogenization temperature vs. calculated salinity of fluid inclusions from the Beiya deposit.

ID2 inclusions than that of ID1 inclusions. This is supported by the fact that quartz in S2 veins displays oscillatory zoning under SEM-CL (Fig. 8D), in contrast to the homogeneous texture of quartz in S1 veins (Fig. 8A). Quartz in S2 veins is coarser and has a more euhedral shape than quartz in S1 veins (Fig. 8A and C), suggesting that the former crystallized in a relatively open environment. This could have been due to increased permeability and a more concentrated fluid flux as the porphyry intrusion became more fractured at a later stage after continuous hydraulic fracturing. The increased H_2S content of the fluids in the S2 veins may have been due to the gradual precipitation of magnetite (indicated by the alteration mineral assemblage) by a reaction such as $9FeCl_2 + SO_2 + 10H_2O \rightarrow 3Fe_3O_4 + H_2S + 18HCl$, suggested by Ulrich et al. (2002). However, the resulting H_2S activity increase was insufficient to cause the saturation of sulfides at such high temperature and is consistent with only minor pyrite precipitation and the general absence of sulfides in the S2 quartz veins.

Continuous hydraulic fracturing and propagation of fractures finally lead to the transition of lithostatic pressure (> 300 bar) to hydrostatic pressure (< 200 bar; Fig. 13) at a depth of ca. 1.5 km. This is indicated by the sharp decrease in the minimum pressure of L3 inclusions in the Stage 3 veins (Fig. 13). The fluid temperature also decreased significantly to ca. 350 °C, and ranged from 248 to 398 °C (Figs. 11–13). The salinity of L3 inclusions decreased from 10 wt% NaCl equiv. to 5 wt % NaCl equiv. (Fig. 13). The L3 fluids may have formed from the contraction of former high-temperature intermediate density aqueous fluids (ID1 and/or ID2) by the process proposed by Heinrich et al. (2004) in response to downward retracting isotherms in the waning hydrothermal system, given the similar CO_2 content of L3 inclusions (4 mol.%) to that in ID1 and ID2 inclusions (Table 2).

5.2. Phase separation and metal transporting medium in the Beiya deposit

Phase separation or boiling is a common process in many subduction-related porphyry deposit systems (Klemm et al., 2007, 2008; Landtwing et al., 2005; Rusk et al., 2008; Ulrich et al., 2002). A high density and salinity brine and a low density and salinity vapor formed during the depressurization of a deep source supercritical intermediate density fluid. The brine was long thought to be the favored ore-forming fluid due to its capacity to dissolve large quantities of base metals as chloride complexes (Cline, 1995; Landtwing et al., 2005; Richards, 2011 and references therein). In the Beiya deposit, ID1 and ID2 inclusions represent the initial stage fluids, with high metal concentrations of 2000–10,000 ppm Fe, 2000–4000 ppm Cu, 200–600 ppm Zn, 200–500 ppm Pb, tens of ppm Mo, several ppm Ag, and 0.9–5.9 ppm Au (Table 3), comparable to subduction-related porphyry deposits, which have average concentrations of 2660 ppm Cu, 600 ppm Zn, 330 ppm Pb, 70 ppm Mo, 30 ppm Ag, and 1.6 ppm Au (Kouzmanov and Pokrovski, 2012). These initial fluids transported the total Au-Fe-Cu-Pb-Zn-Ag endowment from a deeper magma source to shallower parts of the system. The metal contents of the brine and vapor inclusions were differentiated during boiling. The absolute concentrations of most elements in the brine inclusions of both Stage 1 and Stage 2 are higher than those in vapor inclusions (Table 3; Fig. 14A and C), with 9000–24600 ppm Fe, 3400–11,000 ppm Cu, 1200–5200 ppm Pb, 500–3000 ppm Zn, hundreds of ppm Mo, and tens of ppm Ag in brine inclusions. However, the corresponding vapor inclusions can still contain 400–6000 ppm Fe, 1700–4700 ppm Cu, 50–270 ppm Pb, 100–500 ppm Zn, tens of ppm Mo, and several ppm Ag. Relative to major elements (Na and K) in the fluids, some metals are even more enriched in vapor inclusions, such as Cu (Fig. 14B and D and 15B). This is consistent with the fact that, in some subduction-related porphyry deposits, considerable amounts of metals were consistently present in some vapor inclusions (Heinrich, 2005; Klemm et al., 2007, 2008; Ulrich et al., 2002; Williams-Jones et al., 2005). The abundance of brine inclusions in Stage 1 and Stage 2 veins are very small compared with that of vapor inclusions and intermediate density aqueous fluid inclusions. Therefore, low to intermediate density fluids are considered to be the main metal transporting medium in the Beiya metallogenic system. Lewis and Lowell (2009) suggested that the high density and viscosity of saline brines might restrict their flow, leaving them as a dense residual liquid in the deeper parts of an evolving magmatic hydrothermal system. However, lower density vapor-like fluids can be easily migrated upward. This may explain why the smaller amounts of mineralization occurred inside the Beiya porphyry and why most reserves are located at the contact zone and the distal part because the majority of metals are transported out of the porphyry by low to intermediate density fluids.

5.3. Metal precipitation mechanism in the Beiya deposit

During the evolution of magmatic hydrothermal fluids in porphyry systems, processes that may change fluid composition and cause metal precipitation include decompression, phase separation, cooling, interaction with rocks, and mixing with external water (Kouzmanov and Pokrovski, 2012). These processes are interconnected and one may overprint or act in parallel with another.

Almost no metals precipitated during Stage 1 and Stage 2, although extensive phase separation occurred. This is consistent with the

Table 3
Analyses of LA-ICP-MS for elemental concentrations (ppm) for fluid inclusion assemblages of three stages of mineralization in the Beiya deposit.

FIA No.	Na	SD(N)[1]	K	SD(N)	Mn	SD(N)	Fe	SD(N)	Cu	SD(N)	Zn	SD(N)	Rb	SD(N)	Sr	SD(N)	Mo
ID1																	
W15-38-1(6)a	15,295	2062(2)	6039	634(2)	926	(1)	2144	1680(2)	2423	105(2)	244	195(2)	64	39(2)	43	29(2)	< 2[2]
W15-38-1(4)a	19,141	3587(3)	6293	1415(3)	526	(1)	2675	1956(2)	2291	314(3)	349	200(2)	75	66(3)	59	51(3)	< 10
W15-39-2(6)a	25,592	3868(2)	17,248	3794(2)	1204	177(2)	6403	3891(2)	2371	288(2)	632	149(2)	280	49(2)	70	30(2)	59
W15-39-2(5)a	26,093	3395(3)	11,087	976(3)	1555	426(3)	8118	971(3)	2114	145(3)	600	53(3)	197	23(3)	63	64(3)	89
W15-39-2(4)a	19,111	6304(3)	7495	3834(3)	1702	(1)	2436	(1)	1994	504(2)	295	23(2)	94	60(2)	16	10(3)	< 41
W15-40(3)a	13,418	30(2)	4672	212(2)	407	294(2)	1051	(1)	2857	2296(2)	173	162(2)	57	16(2)	24	9(2)	17
W15-40(1)a	17,787	12414(3)	7460	5693(3)	719	(1)	< 8406		2247	1330(3)	493	(1)	72	5(2)	136	(1)	26
W15-47-1(2)a	29,128	3947(3)	8579	669(3)	1312	480(3)	4802	1644(3)	4118	1270(2)	564	70(3)	226	30(3)	61	25(3)	34
W15-47-1(4)a	13,596	3224(2)	4379	515(2)	251	(1)	577	(1)	4225	4184(2)	261	175(2)	98	8(2)	10	(1)	< 60
B1																	
W15-38-1(6)b	101,771	23067(3)	25,239	8316(3)	6115	2660(3)	16,967	5497(3)	5836	1059(3)	1981	847(3)	564	248(3)	335	152(3)	228
W15-38-1(5)a	100,285	34464(3)	27,462	10649(3)	3093	1630(3)	15,659	4377(3)	5326	567(3)	1430	605(3)	433	240(3)	277	70(3)	23
W15-39-2(5)b	104,244	17260(2)	34,335	1309(2)	3932	2330(2)	17,657	3030(2)	4853	884(2)	1538	546(2)	502	162(2)	393	53(2)	128
W15-40(1)b	92,449	20097(2)	38,099	8333(2)	6995	3218(2)	20,742	5477(2)	4446	9(2)	2180	1135(2)	587	111(2)	312	85(2)	79
V1																	
W15-39-2(6)b	14,113	5600(2)	11,635	4720(2)	574	266(2)	2889	1480(2)	3139	370(2)	191	11(2)	127	46(2)	24	5(2)	24
W15-40(1)c	17,411	(1)	7351	(1)	< 566		< 13,024		2625	(1)	493	(1)	< 87		52	(1)	< 40
W15-47-1(3)a	6566	1681(4)	2829	1402(4)	259	26(2)	2926	2311(3)	3557	1540(4)	381	310(3)	58	15(4)	5	2(3)	23
W15-47-1(2)b	13,581	724(2)	4418	637(2)	503	(1)	2712	(1)	1727	729(2)	188	1(2)	85	27(2)	21	5(2)	22
W15-47-1(4)b	13,920	2901(4)	5496	1034(4)	241	174(3)	2554	838(4)	2759	1242(4)	208	107(4)	130	25(4)	14	9(4)	24
ID2																	
W15-10(1)a	25,968	11535(4)	9956	4443(4)	1032	624(3)	4497	1320(2)	3345	411(2)	643	186(3)	209	84(4)	48	41(3)	40
W15-10(7)a	26,410	3416(6)	10,674	3139(6)	576	295(6)	2464	1867(5)	3871	1108(6)	393	134(6)	164	58(6)	46	19(6)	53
W15-10(7)d	25,696	4895(6)	12,490	3360(6)	349	81(3)	1869	671(4)	3296	257(6)	283	151(5)	122	29(6)	36	29(6)	35
W15-10(7)g	26,087	8279(6)	12,469	3284(6)	451	214(5)	2896	2229(6)	4179	1972(4)	364	137(6)	73	35(5)	88	105(6)	45
W15-10(7)i	23,357	6859(6)	17,526	12509(6)	500	161(5)	4219	1351(4)	3454	302(3)	403	46(4)	73	47(6)	33	38(6)	53
W15-10(7)k	29,015	7754(4)	12,384	4757(4)	549	229(4)	4448	1403(3)	3305	257(3)	397	124(4)	186	112(4)	59	37(4)	88
W14-32-3(2)a	25,775	9839(5)	11,952	3352(5)	1112	1295(4)	4617	4731(3)	3705	726(4)	371	271(5)	171	75(5)	78	73(5)	41
W14-32-3(2)c	20,538	2365(2)	11,062	2823(2)	678	152(2)	3328	659(2)	2620	737(2)	373	22(2)	120	52(2)	100	91(2)	38
W14-32-3(3)a	14,035	1844(2)	9543	1264(2)	< 684		3029	(1)	2959	804(2)	220	112(2)	167	24(2)	27	21(2)	30
W14-32-3(3)d	27,433	9501(6)	11,863	5168(6)	399	108(2)	1736	655(6)	2750	538(4)	228	129(6)	131	47(6)	30	32(6)	31
B2																	
W15-10(7)b	98,697	12686(2)	39,644	28640(2)	1305	1115(2)	10,602	2190(2)	10,127	206(2)	806	824(2)	356	417(2)	157	154(2)	275
W15-10(7)e	90,839	8918(2)	43,634	4585(2)	1950	140(2)	12,494	1212(2)	8699	1348(2)	1194	143(2)	397	87(2)	148	15(2)	275
W14-32-3(3)b	106,267	18119(2)	44,739	5578(2)	1370	743(2)	12,687	2368(2)	10,017	1020(2)	735	407(2)	306	170(2)	148	68(2)	222
V2																	
W15-10(1)b	11,787	2142(4)	5503	1282(4)	561	260(4)	2506	960(4)	2455	255(4)	250	87(4)	105	44(4)	26	27(4)	34
W15-10(7)f	21,785	3836(2)	10,348	6692(2)	911	523(2)	431	(1)	3277	307(2)	291	37(2)	50	40(2)	55	69(2)	< 2
W15-10(7)h	21,302	(1)	16,314	(1)	266	(1)	713	(1)	2884	(1)	77	(1)	41	(1)	4	(1)	18
W15-10(7)j	11,843	1045(2)	11,264	3111(2)	198	9(2)	1871	1200(2)	3264	185(2)	153	18(2)	27	11(2)	5	3(2)	26
W15-10(7)l	10,952	(1)	5584	(1)	452	(1)	6015	(1)	4777	(1)	208	(1)	125	(1)	28	(1)	212
W14-32-3(2)b	10,126	7710(3)	5330	4751(4)	358	(1)	1690	1298(2)	2141	838(3)	180	141(3)	77	75(3)	16	14(3)	46
W14-32-3(3)e	13,340	4518(3)	5663	943(3)	< 411		< 1297		3299	278(3)	186	18(2)	44	1(3)	3	2(2)	28
L3																	
W15-2(2)b	23,701	17462(6)	7655	5526(6)	695	235(2)	4316	(1)	520	481(3)	447	56(2)	61	13(2)	115	99(6)	< 155
W15-3-2(1)a	22,113	11470(3)	9366	6026(3)	366	298(3)	2718	(1)	529	241(3)	308	300(3)	79	46(3)	141	142(3)	< 10
W15-3-2(1)b	20,018	1585(2)	5900	4715(2)	511	(1)	2176	(1)	509	129(2)	229	93(2)	63	44(2)	60	45(2)	< 12
W15-3-2(4)a	8987	(1)	4921	(1)	182	(1)	< 1517		119	(1)	96	(1)	22	(1)	30	(1)	< 10
W15-3-2(5)a	28,239	(1)	9979	(1)	521	(1)	2887	(1)	409	(1)	621	(1)	75	(1)	147	(1)	< 6
W15-3-2(5)b	13,834	(1)	4908	(1)	247	(1)	< 2158		223	(1)	236	(1)	24	(1)	37	(1)	< 10

(continued on next page)

Table 3 (*continued*)

FIA No.	Na	SD(N)[1]	K	SD(N)	Mn	SD(N)	Fe	SD(N)	Cu	SD(N)	Zn	SD(N)	Rb	SD(N)	Sr	SD(N)	Mo
W15-3-2(5)c	27,190	13677(3)	9800	4592(3)	417	241(3)	1891	1642(2)	322	89(3)	319	268(3)	79	44(3)	158	133(3)	< 44
W15-3-2(5)e	19,235	13395(4)	7799	8263(4)	1232	1232(2)	2149	(1)	559	230(4)	468	449(3)	83	92(3)	98	98(4)	< 54
FIA No.	Sr	SD(N)	Mo	SD(N)	Ag	SD(N)	Cs	SD(N)	Ba	SD(N)	Au	SD(N)	Pb	SD(N)	Bi	SD(N)	
ID1																	
W15-38-1(6)a	43	29(2)	< 2[2]		< 6		87	78(2)	14	6(2)	< 2		183	132(2)	3	(1)	
W15-38-1(4)a	59	51(3)	< 10		< 18		61	64(3)	19	(1)	< 9		220	158(3)	2	(1)	
W15-39-2(6)a	70	30(2)	59	31(2)	< 14		351	69(2)	41	7(2)	< 6		721	391(2)	12	0(3)	
W15-39-2(5)a	63	64(3)	89	25(3)	5	(1)	269	59(3)	33	10(3)	< 4		378	311(3)	12	2(3)	
W15-39-2(4)a	16	10(3)	< 41		< 37		43	32(3)	43	24(3)	5.9	(1)	149	84(3)	7	(1)	
W15-40(3)a	24	9(2)	17	16(2)	< 16		59	25(2)	22	(1)	< 3		210	201(2)	9	(1)	
W15-40(1)a	136	(1)	26	(1)	< 40		63	54(3)	< 78		< 15		143	110(3)	< 10		
W15-47-1(2)a	61	25(3)	34	24(2)	8	1(2)	33	11(3)	14	6(2)	< 7		588	295(3)	3	0(3)	
W15-47-1(4)a	10	(1)	< 60		< 37		30	20(2)	< 29		< 14		331	284(2)	< 13		
B1																	
W15-38-1(6)b	335	152(3)	228	258(2)	14	3(3)	691	369(3)	208	107(3)	0.2	(1)	3280	1700(3)	23	13(3)	
W15-38-1(5)a	277	70(3)	23	18(3)	20	9(3)	164	182(3)	187	48(3)	< 1		1546	304(3)	11	8(3)	
W15-39-2(5)b	393	53(2)	128	178(2)	22	2(2)	438	538(2)	226	197(2)	< 1		1631	216(2)	18	17(2)	
W15-40(1)b	312	85(2)	79	23(2)	21	7(2)	480	183(2)	328	301(2)	< 2		2199	457(2)	33	19(3)	
V1																	
W15-39-2(6)b	24	5(2)	24	20(2)	< 6		64	13(2)	17	3(2)	< 3		207	163(2)	10	(1)	
W15-40(1)c	52	(1)	< 40		< 67		46	(1)	< 46		< 29		167	(1)	< 16		
W15-47-1(3)a	5	2(3)	23	13(4)	3	0.4(2)	60	33(4)	1	(1)	0.2	(1)	82	86(3)	5	3(3)	
W15-47-1(2)b	21	5(2)	22	(1)	2	(1)	21	2(2)	13	6(2)	< 2		171	15(2)	1	(1)	
W15-47-1(4)b	14	9(4)	24	22(4)	5	2(2)	48	16(4)	8	4(2)	0.4	(1)	218	85(4)	3	2(4)	
ID2																	
W15-10(1)a	48	41(3)	40	(1)	5	(1)	251	125(4)	34	26(2)	1.2	(1)	267	270(4)	2	(1)	
W15-10(7)a	46	19(6)	53	27(3)	4	2(3)	46	44(6)	18	10(6)	0.9	(1)	348	141(6)	3	3(4)	
W15-10(7)d	36	29(6)	35	24(4)	2	0.3(2)	50	61(6)	8	2(4)	< 2		267	192(6)	2	0.3(3)	
W15-10(7)g	88	105(6)	45	69(6)	3	3(4)	18	22(5)	71	82(4)	< 8		348	115(6)	2	1(3)	
W15-10(7)i	33	38(6)	53	15(3)	1	(1)	24	22(6)	10	3(3)	< 3		219	140(5)	2	1(2)	
W15-10(7)k	59	37(4)	88	40(3)	5	(1)	58	60(4)	12	4(4)	< 2		384	166(4)	4	1(2)	
W14-32-3(2)a	78	73(5)	41	24(4)	6	(1)	87	104(5)	49	48(3)	< 3		318	213(5)	3	2(5)	
W14-32-3(2)c	100	91(2)	38	(1)	3	(1)	92	79(2)	56	68(2)	< 1		323	78(2)	4	4(2)	
W14-32-3(3)a	27	21(2)	30	(1)	< 15		10	(1)	< 10		< 6		175	26(2)	3	(1)	
W14-32-3(3)d	30	32(6)	31	14(5)	8	(1)	31	42(6)	8	3(2)	< 6		242	117(6)	1	(1)	
B2																	
W15-10(7)b	157	154(2)	275	53(2)	16	2(2)	35	42(2)	47	42(2)	0.7	(1)	1478	171(2)	8	(1)	
W15-10(7)e	148	15(2)	275	74(2)	11	3(2)	41	5(2)	44	6(2)	< 1		1270	80(2)	6	0.5(6)	
W14-32-3(3)b	148	68(2)	222	20(2)	8	2(2)	33	19(2)	42	16(2)	< 1		1285	109(2)	5	0.3(2)	
V2																	
W15-10(1)b	26	27(4)	34	12(3)	4	1(2)	109	43(4)	18	19(3)	0.6	(1)	198	57(4)	3	1(4)	
W15-10(7)f	55	69(2)	< 2		6	2(2)	18	9(2)	39	47(2)	< 3		270	54(2)	< 2		
W15-10(7)h	4	(1)	18	(1)	< 1		7	(1)	< 1		< 1		48	(1)	< 1		
W15-10(7)j	5	3(2)	26	(1)	< 3		20	(1)	< 5		< 1		95	27(2)	< 1		
W15-10(7)l	28	(1)	212	(1)	6	(1)	118	(1)	11	(1)	< 1		180	(1)	20	(1)	
W14-32-3(2)b	16	14(3)	46	(1)	5	(1)	9	6(3)	15	(1)	< 7		169	112(3)	3	2(2)	
W14-32-3(3)e	3	2(2)	28	(1)	< 10		6	(1)	5	(1)	< 3		99	80(3)	< 4		
L3																	
W15-2(2)b	115	99(6)	< 155		< 252		59	47(3)	183	86(4)	< 142		400	325(6)	7	1(3)	
W15-3-2(1)a	141	142(3)	< 10		14	(1)	72	50(3)	81	73(3)	< 10		305	281(3)	7	5(3)	
W15-3-2(1)b	60	45(2)	< 12		< 24		63	(1)	54	30(2)	< 11		270	15(2)	< 7		

(*continued on next page*)

Table 3 (*continued*)

FIA No.	Na	SD(N)[1]	K	SD(N)	Mn	SD(N)	Fe	SD(N)	Cu	SD(N)	Zn	SD(N)	Rb	SD(N)	Sr	SD(N)	Mo
W15-3-2(4)a	30	(1)	< 10		< 15		16	(1)	35	(1)	< 6		82	(1)	7	(1)	
W15-3-2(5)a	147	(1)	< 6		< 13		46	(1)	124	(1)	< 5		593	(1)	3	(1)	
W15-3-2(5)b	37	(1)	< 10		< 22		43	(1)	45	(1)	< 7		380	(1)	< 5		
W15-3-2(5)c	158	133(3)	< 44		< 24		46	18(3)	123	102(3)	< 13		332	234(3)	< 3		
W15-3-2(5)e	98	98(4)	< 54		< 72		71	72(4)	62	37(4)	< 36		261	212(4)	38	(1)	

Data are reported as assemblage averages.

[1] SD(N): Standard deviation (SD) and the number of inclusion per assemblage (N).

[2] < 2: The concentration of corresponding element is below the detection limit, e.g. Mo concentration in W15-38-1(6)a is less than 2 ppm.

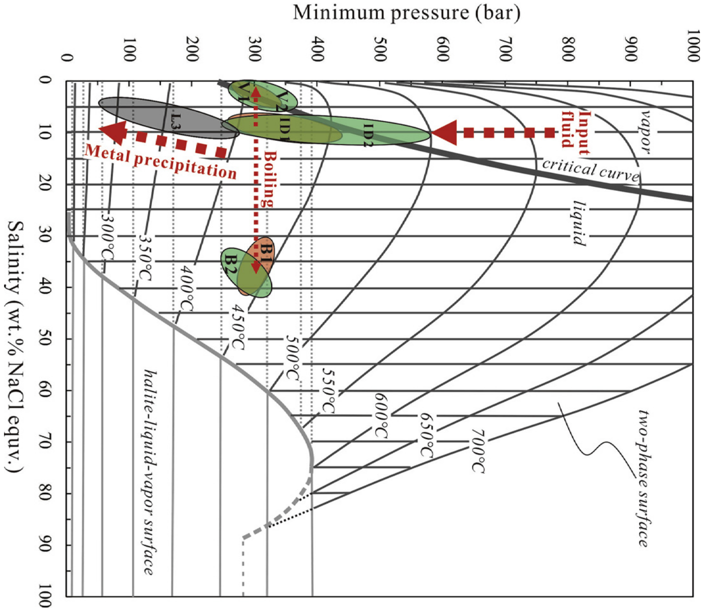

Fig. 13. P-T-salinity phase diagram showing the evolutionary path of hydrothermal fluids within the Beiya deposit (after Driesner and Heinrich, 2007).

consistently high metal concentration of fluid inclusions in S1 and S2 veins, except for Fe, as there were large variations of the Fe/(Na + K) ratio (Fig. 15A). This may have been caused by minor precipitation of magnetite during potassic alteration, resulting in decreased Fe concentrations in some early fluids. Formation of ore minerals, electrum and chalcopyrite, in S3 veins (Fig. 6) is consistent with the sharp decrease of absolute Cu concentration and Cu/(Na + K) ratio in L3 inclusions (Fig. 15B). Mo, Au, and most Ag concentrations of L3 inclusions are all below the detection limit, indicating a dramatic decrease of these metals in these fluids. Phase separation did not occur during Stage 3, as indicated by the single liquid-rich fluid inclusion assemblage. In addition, L3 inclusions contain similarly nonreactive elemental ratios, such as Pb/(Na + K), Zn/(Na + K), Rb/(Na + K), and Cs/(Na + K), to fluid inclusions in the early stages (Fig. 15C–F), indicative of L3 inclusions without dilution by an external fluid (e.g. meteoric water) during metal precipitation (c.f. Audétat and Pettke, 2003; Audétat et al., 2008; Catchpole et al., 2011). This is consistent with the similar magmatic C—O and S isotopic characteristics of calcite and sulfide in different stages of the Beiya deposit reported by Wu et al. (2010). Therefore, the major processes involved in S3 vein formation may have included cooling, pressure reduction, and wall-rock interaction.

Pressure reduction of fluids may affect mineral solubility, e.g., the solubility of quartz decreases with decreasing pressure at a given temperature (Fournier, 1999). However, quantifying this effect on the solubility of sulfide minerals is difficult due to the lack of experimental data. Moreover, decompression typically occurs together with cooling, which increases the difficulty of identifying the contribution of pressure to metal precipitation. However, the effect of pressure on metal solubility in the fluids within the range of depths relevant to the formation of porphyry deposits (< 10 km) may be small due to the low compressibility of liquids at a density > 0.4 g/cm^3 (Kouzmanov and Pokrovski, 2012). Most inclusions in the Beiya deposit have a density of > 0.4 g/cm^3 (Table 2), indicative of little contribution of depressurization to metal precipitation. Cooling of magmatic fluids (to ca. 350 °C) is thought to be the most effective precipitation mechanism in the Beiya deposit, consistent with what has been proposed for many subduction-related porphyry deposits such as the Bingham Canyon

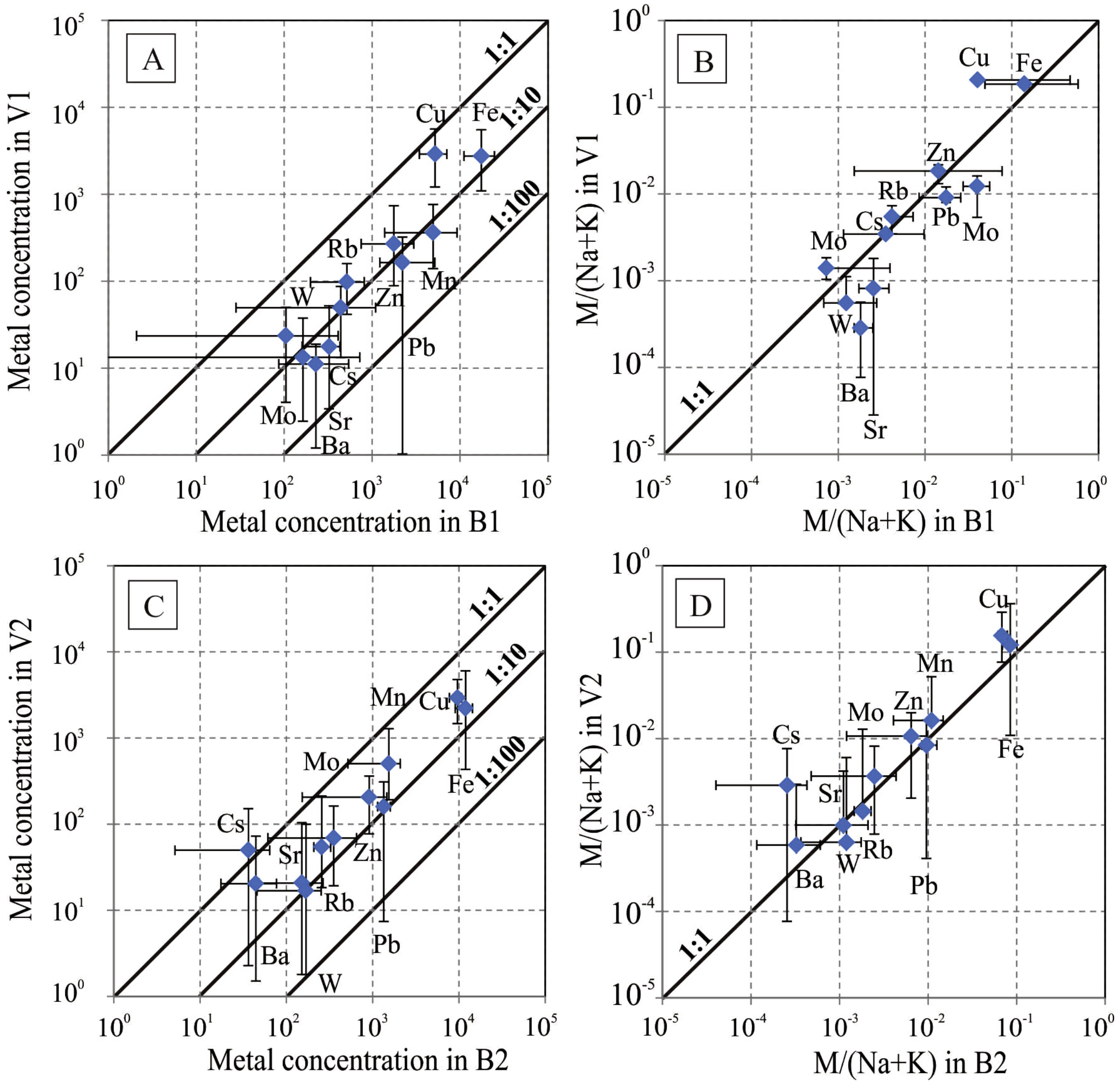

Fig. 14. Binary diagrams illustrating metal differentiation during phase separation. (A and C) Absolute metal concentration in vapor inclusions versus absolute metal concentration in brine inclusions of Stage 1 and Stage 2 veins, respectively; (B and D) M/(Na + K) in vapor inclusions vs. M/(Na + K) in brine inclusions of Stage 1 and Stage 2 veins, respectively. M is the corresponding metal concentration. The error bar represents the upper and lower limits of metal concentration or the M/(Na + K) ratio.

deposit (Landtwing et al., 2005), Butte deposit (Rusk et al., 2004), and Morococha deposit (Catchpole et al., 2011). This is confirmed by thermodynamic calculations showing that sulfide mineral solubility decreases with decreasing temperature (Kouzmanov and Pokrovski, 2012 and references therein). In addition, cooling of a magmatic fluid is accompanied by large changes in sulfur speciation, by disproportionation of SO_2 to H_2S and sulfuric acid, which in turn affects H_2S concentration and acidity. SO_2 would mostly breakdown and H_2S concentrations of fluids would increase if H^+ could be consumed effectively, e.g., consumed by silicate minerals during phyllic alteration in porphyry deposits (Richards, 2011). The increase of H_2S concentrations may lead to precipitation of ore minerals. The most efficient mechanism for the precipitation of Zn and Pb is the neutralization of an acidic fluid by interaction with wall rocks at both high and low temperatures (Kouzmanov and Pokrovski, 2012). However, this is unfeasible in relatively non-reactive porphyry environments, resulting in migration and precipitation of Pb and Zn to the distal parts of the system. However, S3 veins connect to the late stage skarn ores (Fig. 5G), where carbonate wall rocks can consume acid more effectively, leading to precipitation of metals in the giant Beiya Au deposit.

6. Conclusions

A detailed study of petrography, microthermometry and compositions of fluid inclusions from three different hydrothermal stages allows us to draw the following conclusions.

1. Three hydrothermal stages are recorded in the Beiya Au deposit. Stage 1 and Stage 2 veins contain three types of fluid inclusions: intermediate density aqueous inclusions, high density brine inclusions, and low density vapor inclusions. Stage 3 veins contain only liquid-rich fluid inclusions. All fluids belong to the H_2O-NaCl-CO_2 hydrothermal system.
2. The initial magma-derived intermediate density aqueous fluids were condensed to form a low-density vapor and high-density brine during ascent to 1.5 km at 400 °C and 300 bar. The low to

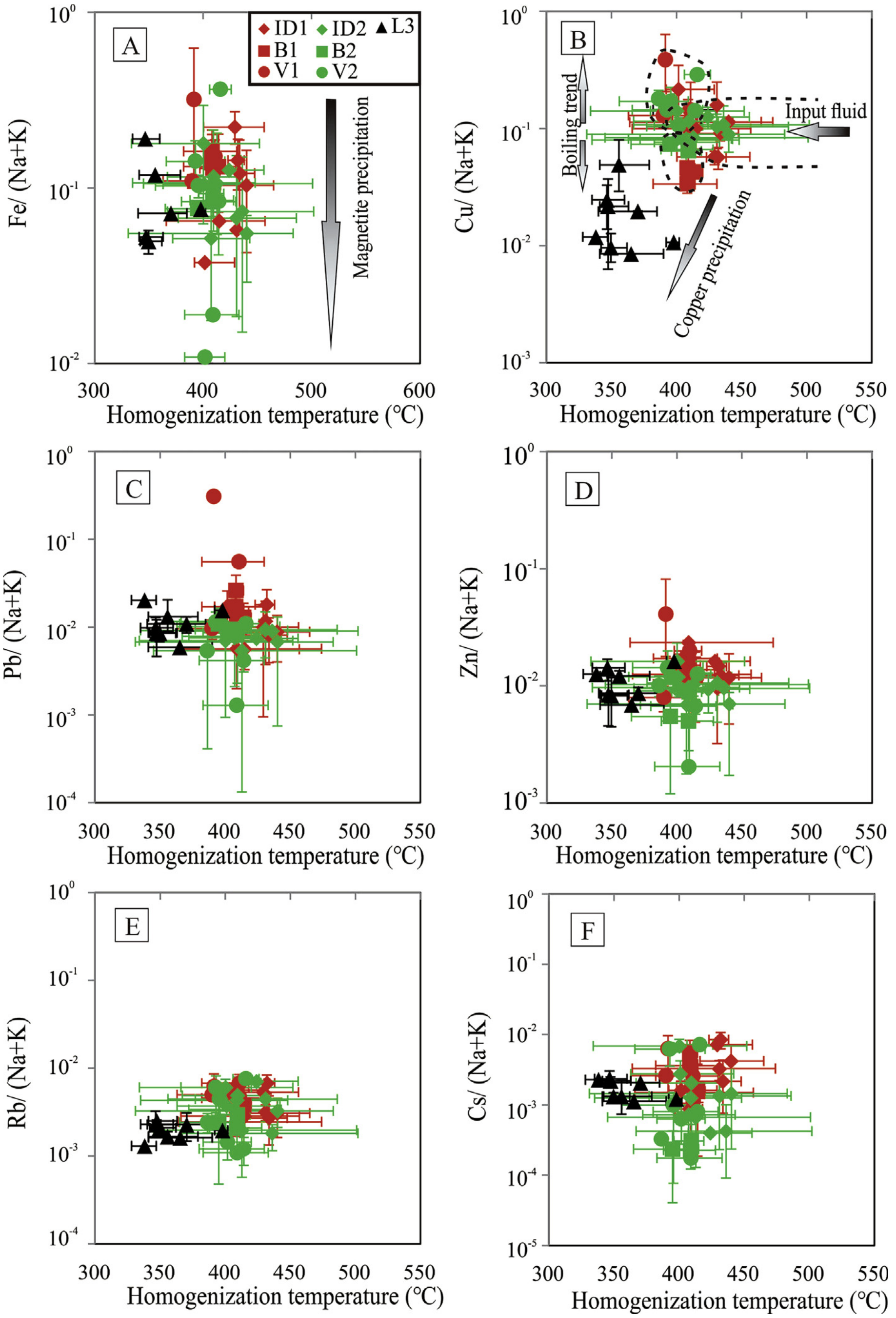

Fig. 15. Binary diagrams illustrating elemental ratios of fluid inclusions vs. homogenization temperature diagrams for ore metals and non-reactive elements. (A) Fe/(Na + K) vs. temperature; (B) Fe/(Na + K) vs. temperature; (C) Fe/(Na + K) vs. temperature; (D) Fe/(Na + K) vs. temperature; (E) Fe/(Na + K) vs. temperature; (F) Fe/(Na + K) vs. temperature. The error bar represents the upper and lower limits of the metal M/(Na + K) ratio, where M is the corresponding metal concentration.

intermediate density fluids were abundant, had very high metal contents and were the most important medium for metal transport.

3. Ore metals were precipitated at a relatively low hydrostatic pressure (< 200 bar) and low temperature of approximately 350 °C. Cooling of hydrothermal fluids was the most important trigger for metal precipitation in the Beiya deposit.

Acknowledgments

We are grateful to Engineer Zhangrong Liu for help during field investigations and to Shaohua Dong, Jiali Cai, Chaojian Qin, and Yanwen Tang for assistance in the laboratory. Professor Mei-Fu Zhou, Professor A. Williams-Jones and an anonymous reviewer are thanked for their constructive comments and suggestions that helped to improve the manuscript. This study was financially supported by the Strategic Priority Research Program (B) of Chinese Academy of Sciences (XDB18000000), the Natural Science Foundation of China (41473052), the High-level innovative talents training plan of Guizhou province (2016: 5681), and the Key Natural Science Foundation of China (41130423).

References

Allan, M.M., 2005. Validation of LA-ICP-MS fluid inclusion analysis with synthetic fluid inclusions. Am. Mineral. 90, 1767–1775.
Audétat, A., Pettke, T., 2003. The magmatic-hydrothermal evolution of two barren granites: a melt and fluid inclusion study of the Rito del Medio and Cañada Pinabete

plutons in northern New Mexico (USA). Geochim. Cosmochim. Acta 67, 97–121.

Audétat, A., Pettke, T., Heinrich, C.A., Bodnar, R.J., 2008. The composition of magmatic-hydrothermal fluids in barren versus mineralized intrusions. Econ. Geol. 103, 877–908.

Bakker, R.J., 1997. Clathrates: Computer Programs to Calculate Fluid Inclusion V-X Properties using Clathrate Melting Temperatures. Pergamon Press, Inc.

Bi, X.W., Hu, R.Z., Hanley, J.J., Mungall, J.E., Peng, J.T., Shang, L.B., Wu, K.X., Shuang, Y., Li, H.L., Hu, X.Y., 2009. Crystallization conditions (T, P, fO_2) from mineral chemistry of Cu- and Au-mineralized alkaline intrusions in the Red River-Jinshajiang alkaline igneous belt, western Yunnan Province, China. Mineral. Petrol. 96, 43–58.

Bi, X.W., Hu, R.Z., Peng, J.T., Wu, K.X., Su, W.C., Zhan, X.Z., 2005. Geochemical characteristics of the Yao'an and Machangqing alkaline-rich intrusions. Acta Petrol. Sin. 21, 113–124.

Bi, X.W., Hu, R.Z., Cornell, D.H., 2004. The alkaline porphyry associated Yao'an gold deposit, Yunnan, China: rare earth element and stable isotope evidence for magmatic hydrothermal ore formation. Mineral. Depos. 39, 21–30.

Bodnar, R.J., Vityk, M.O., 1994. Interpretation of microthermometric data for H2O-NaCl fluid inclusions: Short Course of Working Group (IMA) in“Inclusions in Minerals,” Pontignano-Siena. 1–4 September 1994, 117–130.

Brown, P.E., Lamb, W.M., 1989. P-V-T properties of fluids in the system $H_2O \pm CO_2 \pm NaCl$: new graphical presentations and implications for fluid inclusion studies. Geochim. Cosmochim. Acta 53, 1209–1221.

Catchpole, H., Kouzmanov, K., Fontboté, L., Guillong, M., Heinrich, C.A., 2011. Fluid evolution in zoned Cordilleran polymetallic veins-Insights from microthermometry and LA-ICP-MS of fluid inclusions. Chem. Geol. 281, 293–304.

Cline, J.S., 1995. Genesis of porphyry copper deposits: the behavior of water, chloride, andcopper in crystallizing melts. In: Pierce, F.W., Bolm, J.G. (Eds.), Porphyry Copper Deposits of the American Cordillera: Arizona Geological Society Digest, 20, pp. 69–82.

Cooke, D.R., 2005. Giant porphyry deposits: characteristics, distribution, and tectonic controls. Econ. Geol. 100 (5), 801–818.

Deng, J., Wang, Q., Li, G., Hou, Z., Jiang, C., Danyushevsky, L., 2015. Geology and genesis of the giant Beiya porphyry-skarn gold deposit, northwestern Yangtze Block, China. Ore Geol. Rev. 70, 457–485.

Deng, J., Wang, Q., Li, G., Santosh, M., 2014. Cenozoic tectono-magmatic and metallogenic processes in the Sanjiang region, southwestern China. Earth-Sci. Rev. 138, 268–299.

Diamond, L.W., Tarantola, A., Stünitz, H., 2010. Modification of fluid inclusions in quartz by deviatoric stress. II: experimentally induced changes in inclusion volume and composition. Contrib. Mineral. Petrol. 160, 845–864.

Driesner, T., Heinrich, C.A., 2007. The system H_2O-NaCl. Part I. Correlation formulae for phase relations in temperature-pressure-composition space from 0 to 1000°C, 0 to 5000 bar, and 0 to 1 XNaCl. Geochim. Cosmochim. Acta 71, 4880–4901.

Duan, Z., Møller, N., Weare, J.H., 1992. An equation of state for the CH_4-CO_2-H_2O system: II. Mixtures from 50 to 1000°C and 0 to 1000 bar. Geochim. Cosmochim. Acta 56, 2619–2631.

Fournier, R.O., 1999. Hydrothermal processes related to movement of fluid from plastic into brittle rock in the magmatic-epithermal environment. Econ. Geol. Bull. Soc. Econ. Geol. 94, 1193–1211.

Fu, Y., Sun, X., Zhou, H., Lin, H., Jiang, L., Yang, T., 2017. In-situ LA-ICP-MS trace elements analysis of scheelites from the giant Beiya gold-polymetallic deposit in Yunnan Province, Southwest China and its metallogenic implications. Ore Geol. Rev. 80, 828–837.

Fu, Y., Sun, X., Lin, H., Zhou, H., Li, X., Quyang, X., Jiang, L., Shi, G., Liang, Y., 2015. Geochronology of the giant Beiya gold-polymetallic deposit in Yunnan Province, Southwest China and its relationship with the petrogenesis of alkaline porphyry. Ore Geol. Rev. 71, 138–149.

Fu, Y., Sun, X., Zhou, H., Lin, H., Yang, T., 2016. In-situ LA–ICP–MS U-Pb geochronology and trace elements analysis of polygenetic titanite from the giant Beiya gold–-polymetallic deposit in Yunnan Province, Southwest China. Ore Geol. Rev. 77, 43–56.

Goldstein, R.H., Reynolds, T.J., 1994. Systematics of fluid inclusions in diagenetic minerals: Society of Sedimentary Geology, SEPM Short Course 31, 199 p.

Guillong, M., Meier, D.L., Allan, M.M., Heinrich, C.A., Yardley, B.W.D., 2008. SILLS: A MATLAB-based program for the reduction of laser ablation ICP-MS data of homogeneous materials and inclusions. In: Sylvester, P. (Ed.), Laser Ablation ICP-MS in the Earth Sciences: Current Practices and Outstanding Issues. Mineralogical Association of Canada Short Course Series 40, pp. 328–333.

He, W., Yang, L., Mccuaig, T.C., Lu, Y., Brugger, J., Bao, X., Gao, X., Lu, Y., Xing, Y., 2016. Hydrothermal evolution and ore genesis of the Beiya giant Au polymetallic deposit, western Yunnan, China: evidence from fluid inclusions and H-O-S-Pb isotopes. Ore Geol. Rev. http://dx.doi.org/10.1016/j.oregeorev.2016.10.035.

He, W., Mo, X., He, Z., White, N.C., Yang, K., Wang, R., Yu, X., Dong, G., Huang, X., 2015. The geology and mineralogy of the Beiya skarn gold deposit in Yunnan, Southwest China. Econ. Geol. 110, 1625–1641.

He, Z., Zhou, Y.M., He, W., Su, G., Li, W., Yang, S., 2013. Genetic types and metallogenic regularity of Beiya superlarge gold-polymetallic deposit, northwestern Yunnan. Mineral Depos. 32, 244–258 (in Chinese with English abstracts).

Hedenquist, J.W., Arribas, A., Reynolds, T.J., 1998. Evolution of an intrusion-centered hydrothermal system: far southeast-lepanto porphyry and epithermal Cu-Au deposits, Philippines. Economic Geology 93, 373–404.

Heinrich, C.A., 2007. Fluid-fluid interactions in magmatic-hydrothermal ore formation. Rev. Mineral. Geochem. 65, 363–387.

Heinrich, C.A., 2005. The physical and chemical evolution of low-salinity magmatic fluids at the porphyry to epithermal transition: a thermodynamic study. Mineralium Depos. 39, 864–889.

Heinrich, C.A., Driesner, T., Stefánsson, A., Seward, T.M., 2004. Magmatic vapor contraction and the transport of gold from the porphyry environment to epithermal ore deposits. Geology 32, 761–764.

Heinrich, C.A., Pettke, T., Halter, W.E., Aigner-Torres, M., Audétat, A., Günther, D., Hattendorf, B., Bleiner, D., Guillong, M., Horn, I., 2003. Quantitative multi-element analysis of minerals, fluid and melt inclusions by laser-ablation inductively-coupled-plasma mass-spectrometry. Geochim. Cosmochim. Acta 67, 3473–3497.

Hou, Z.Q., Yang, Z.M., Qu, X.M., Meng, X.J., Li, Z.Q., Beaudoin, G., Rui, Z.Y., Gao, Y.F., Zaw, K., 2009. The Miocene Gangdese porphyry copper belt generated during post-collisional extension in the Tibetan orogen. Ore Geol. Rev. 36, 25–51.

Hou, Z.Q., Xie, Y.L., Xu, W.Y., Li, Y.Q., Zhu, X.K., KhinZaw, Beaudoin, G., Rui, Z.Y., Huang, W., LuobuCiren, 2007. Yulong Deposit, Eastern Tibet: a high-sulfidation Cu-Au porphyry copper deposit in the Eastern Indo-Asian Collision Zone. Int. Geol. Rev. 49, 235–258.

Hou, Z.Q., Zhong, D.L., Deng, W.M., 2004. A tectonic model for porphyry copper-molybdenum-gold metallogenic belts on the eastern margin of the Qinghai-Tibet Plateau. Chinese Geol. 31, 1–14 (in Chinese with English abstracts).

Hu, R.Z., Burnard, P.G., Bi, X.W., Zhou, M.F., Pen, J.T., Su, W.C., Wu, K.X., 2004. Helium and argon isotope geochemistry of alkaline intrusion-associated gold and copper deposits along the Red River-Jinshajiang fault belt, SW China. Chem. Geol. 203, 305–317.

Klemm, L.M., Pettke, T., Heinrich, C.A., 2008. Fluid and source magma evolution of the Questa porphyry Mo deposit, New Mexico, USA. Mineralium Depos. 43, 533–552.

Klemm, L.M., Pettke, T., Heinrich, C.A., Campos, E., 2007. Hydrothermal evolution of the El Teniente Deposit, Chile: porphyry Cu-Mo Ore deposition from low-salinity magmatic fluids. Econ. Geol. 102, 1021–1045.

Kouzmanov, K., Pokrovski, G.S., 2012. Hydrothermal controls on metal distribution in porphyry Cu (-Mo-Au) systems. SEG Special Publication 16: Geology and genesis of major copper deposits and districts of the world: A tribute to Richard H. Sillitoe.

Lan, T.G., Hu, R.Z., Bi, X.W., Mao, G.J., Wen, B.J., Liu, L., Chen, Y.H., 2017a. Metasomatized asthenospheric mantle contributing to the generation of Cu-Mo deposits within an intracontinental setting: a case study of the ∼128 Ma Wangjiazhuang Cu-Mo deposit, eastern North China Craton. J. Asian Earth Sci. http://dx.doi.org/10.1016/j.jseaes.2017.07.014.

Lan, T.G., Hu, R.Z., Fan, H.R., Bi, X.W., Tang, Y.W., Zhou, L., Mao, W., Chen, Y.H., 2017b. In-situ analysis of major and trace elements in fluid inclusion and quartz: LA-ICP-MS method and applications to ore deposits. Acta Petrol. Sin. 33, 3239–3262 (in Chinese with English abstracts).

Landtwing, M., Pettke, T., Halter, W., Heinrich, C., Redmond, P., Einaudi, M., Kunze, K., 2005. Copper deposition during quartz dissolution by cooling magmatic-hydrothermal fluids: The Bingham porphyry. Earth Planet. Sci. Lett. 235, 229–243.

Lewis, K.C., Lowell, R.P., 2009. Numerical modeling of two-phase flow in the NaCl-H_2O system: introduction of a numerical method and benchmarking. J. Geophys. Res. Solid Earth 114. http://dx.doi.org/10.1029/2008JB006030 16 pp., B08204.

Li, W.C., Wang, J.H., He, Z.H., Dou, S., 2016. Formation of Au-polymetallic ore deposits in alkaline porphyries at Beiya, Yunnan, Southwest China. Ore Geol. Rev. 73, 241–252.

Liu, B., Liu, H., Zhang, C., Mao, Z., Zhou, Y., Huang, H., He, Z., Su, G., 2015. Geochemistry and geochronology of porphyries from the Beiya gold-polymetallic orefield, western Yunnan, China. Ore Geol. Rev. 69, 360–379.

Liu, Z., Liao, S.Y., Wang, J.R., Ma, Z., Liu, Y.X., Wang, D.B., Tang, Y., Yang, J., 2017. Petrogenesis of late Eocene high Ba-Sr potassic rocks from western Yangtze Block, SE Tibet: a magmatic response to the Indo-Asian collision. J. Asian Earth Sci. 135, 95–109.

Lu, Y.J., Robert, K., Anthony, I.S., 2013. Intercontinental Eocene-Oligocene porphyry Cu mineral system of Yunnan, western Yangtze craton, China: compositional characteristics, sources, and implications for continental collision metallogeny. Econ. Geol. 108, 1541–1576.

Richards, J.P., 2011. Magmatic to hydrothermal metal fluxes in convergent and collided margins. Ore Geol. Rev. 40, 1–26.

Roedder, E., 1967. Fluid inclusions as samples of ore fluids. In: Barnes, H.L. (Ed.), Geochemistry of Hydrothermal Ore DepositsNew York. Holt, Rinehart and Winston, pp. 515–574.

Rusk, B.G., Reed, M.H., Dilles, J.H., 2008. Fluid inclusion evidence for magmatic-hydrothermal fluid evolution in the porphyry copper-molybdenum deposit at Butte, Montana. Econ. Geol. 103, 307–334.

Rusk, B.G., Reed, M.H., Dilles, J.H., Klemm, L.M., Heinrich, C.A., 2004. Compositions of magmatic hydrothermal fluids determined by LA-ICP-MS of fluid inclusions from the porphyry copper-molybdenum deposit at Butte, MT. Chem. Geol. 210, 173–199.

Sillitoe, R.H., 2010. Porphyry copper systems. Econ. Geol. 105, 3–41.

Ulrich, T., Gunther, D., Heinrich, C.A., 2002. The evolution of a porphyry Cu-Au deposit, based on LA-ICP-MS analysis of fluid inclusions: Bajo de la Alumbrera, Argentina. Econ. Geol. 97, 1889–1920.

Wang, D., Bi, X., Lu, H., Hu, R., Wang, X., Xu, L., 2017. Fluid and melt inclusion study on mineralized and barren porphyries, jinshajiang-red river alkali-rich intrusive belt, and significance to metallogenesis. J. Geochem. Explor. 184, 28–39.

Williams-Jones, A.E., Heinrich, C.A., Migdisov, A.A., 2005. Vapor as a medium for the transport of metals: implications for ore deposit modeling. Geochim. Cosmochim. Acta Suppl. 69.

Wilkinson, J.J., 2001. Fluid inclusions in hydrothermal ore deposits. Lithos 55, 229–272. http://dx.doi.org/10.1016/S0024-4937(00)00047-5.

Wu, K.X., Hu, R.Z., Bi, X.W., Peng, J.T., 2010. An oxygen and carbon isotope study on the formation mode of calcite in beiya gold deposit, west yunnan province, China. Acta Mineral. Sin. 30, 463–469 (in Chinese with English abstracts).

Xu, L., Bi, X., Hu, R., Qi, Y., Tang, Y., Wang, X., Zhu, J., 2016. Redox states and genesis of magmas associated with intra-continental porphyry Cu–Au mineralization within the Jinshajiang-Red River alkaline igneous belt, SW China. Ore Geol. Rev. 73, 330–345.

Xu, L., Bi, X., Hu, R., Tang, Y., Wang, X., Xu, Y., 2015. LA-ICP-MS mineral chemistry of titanite and the geological implications for exploration of porphyry Cu deposits in the Jinshajiang-Red River alkaline igneous belt, SW China. Mineral. Petrol. 109, 181–200.

Xu, L., Bi, X., Hu, R., Tang, Y., Jiang, G., Qi, Y., 2014. Origin of the ore-forming fluids of the Tongchang porphyry Cu-Mo deposit in the Jinshajiang-Red River alkaline igneous belt, SW China: constraints from He, Ar and S isotopes. J. Asian Earth Sci. 79, 884–894.

Xu, L., Bi, X., Hu, R., Zhang, X., Su, W., Qu, W., Hu, Z., Tang, Y., 2012. Relationships between porphyry Cu–Mo mineralization in the Jinshajiang-Red River metallogenic belt and tectonic activity: constraints from zircon U-Pb and molybdenite Re–Os geochronology. Ore Geol. Rev. 48, 460–473.

Xu, X.W., Zhang, B.L., Qin, K.Z., Mao, Q., Cai, X.P., 2007. Origin of lamprophyres by the mixing of basic and alkaline melts in magma chamber in Beiya area, western Yunnan, China. Lithos 99, 339–362.

Xu, X.W., Cai, X., Song, B., Zhang, B., Ying, H., Xiao, Q., Wang, J., 2006. Petrologic, chronological and geochemistry characteristics and formation mechanism of alkaline porphyries in the Beiya gold district, western Yunnan. Acta Petrol. Sin. 22, 631–642 (in Chinese with English abstracts).

Yang, R., He, Z.H., Wang, C.M., 2014. The Reserve Investigation Report of the Beiya Gold Deposit, Heqing. Yunnan Gold and Mineral Group Corp. Heqing. Yunnan Gold and Mineral Group Corp., Yunnan (in Chinese).

Zhang, Y.G., Frantz, J.D., 1987. Determination of the homogenization temperatures and densities of supercritical fluids in the system NaCl-KCl-$CaCl_2$-H_2O using synthetic fluid inclusions. Chem. Geol. 64, 335–350.

Zhou, H., Sun, X., Cook, N.J., Lin, H., Fu, Y., Zhong, R., Brugger, J., 2017. Nano- to micron-scale particulate gold hosted by magnetite: a product of gold scavenging by bismuth melts. Econ. Geol. 112, 993–1010.

Zhou, H., Sun, X., Fu, Y., Lin, H., Jiang, L., 2016. Mineralogy and mineral chemistry of Bi-minerals: constraints on ore genesis of the Beiya giant porphyry-skarn gold deposit, southwestern China. Ore Geol. Rev. 79, 408–424.